This is to certify that the
dissertation entitled

SCANNING PROBE STUDY OF A TWO-DIMENSIONAL ELECTRON SYSTEM AND DONOR LAYER CHARGING IN HETEROSTRUCTURED SEMICONDUCTORS

presented by

IRMA KULJANISHVILI

has been accepted towards fulfillment
of the requirements for the

Ph.D. degree in PHYSICS

Steven Tessmer
Major Professor's Signature

October 28, 2005
Date

MSU is an Affirmative Action/Equal Opportunity Institution

SCANNING PROBE STUDY OF A TWO-DIMENSIONAL ELECTRON SYSTEM AND DONOR LAYER CHARGING IN HETEROSTRUCTURED SEMICONDUCTORS

By

Irma Kuljanishvili

A DISSERTATION

Submitted to
Michigan State University
In partial fulfillment of the requirements
For the degree of

DOCTOR OF PHILOSOPHY

Department of Physics and Astronomy

2005

ABSTRACT

SCANNING PROBE STUDY OF TWO-DIMENSIONAL ELECTRON SYSTEMS AND DONOR LAYER CHARGING IN HETEROSTRUCTURED SEMICONDUCTORS

By

Irma Kuljanishvili

We have applied a novel scanned probe method called charge accumulation imaging (CAI) to study two electronic systems in GaAs/AlGaAs heterostructured crystals: two-dimensional electron systems (2DES), and dopant Si atoms confined to a single monolayer. In a presence of magnetic field we have imaged the 2DES at half-filled Landau level and observed evidence of intriguing density modulation induced structure of wavelength 200 nm. The direction of this stripe-like structure is approximately 35 degree to the [110] crystalline axis, which is different from the easy direction of the electronic transport based on measurements performed by other research groups. The nature of this density variation is unclear; however, it may be related to a charge density wave picture predicted theoretically. We have also probed the donor layer charging in gallium arsenide as a function of bias voltage and magnetic field. In a tunneling regime, we have studied the electronic energy spectrum of donor atoms and resolved individual electrons entering the system. We interpret our experimental results in terms of a donor molecule model. To the best of our knowledge , this is the first scanning probe study of donor atom energy levels.

This thesis is dedicated to my parents.

ACKNOWLEDGEMENTS

There is large number of people whom I would like to thank here for their support and assistance. This work would be impossible without their presence in various stages of my journey. First of all, I would like to thank my thesis adviser Professor Stuart Tessmer who took me aboard his group several years ago. All through these years, he has been very supporting and encouraging teacher, optimistic and directing supervisor. I am very fortunate to have an opportunity to work with him. Personal qualities of his character and love for science made my research experience in the group professional on one hand and friendly on the other. I consider myself very lucky to have a chance to be working under his supervision.

I am very grateful to Professors Carlo Piermarocchi and Tom Kaplan for their interest in my research. Their expert theoretical input was very helpful in the process of understanding the interesting physics of my latest experimental finding.

For the years spent in this Department, I have to thank all my teachers whom I respect deeply and thank them for their help. I would like to start with Prof. Susan Simkin who was the first person I met here in the department. She helped me with numerous advice and motherly care during my very first interactions with different culture and customs. I will always be deeply thankful to her for that. I would like to thank Prof. Beers, with whom I worked on several occasions as an Astronomy teaching assistant and from whom I have learned at lot of Astronomy: I deeply respect him as a person and a very good scientist. I would also like to thank Prof. Stein at Astronomy department, with whom I also worked as a teaching assistant, and whose pedagogical wisdom taught me

how to be a better teacher. I would also like to thank all Professors who taught us all classes and shared their expert knowledge of physics with us-graduate students: Prof. Mahanti, Prof. Bass, Prof. Zelevinsky, Prof. Dykman, Prof. Birge, Prof. Stump, Prof. Harrison, Prof. Pollack, Prof. Billinge, Prof. Repko, Prof. Kovacs and others. They helped me learn how to be most successful in the classroom, which is a very important part in every student's life, especially the PhD students.

I would like to attribute my special thanks to all members of our group starting with Illari Maasilta, a former Post-Doc in our group. To all my lab-mates through the years starting from the beginning: Sergei Urazhdin, the first graduate student in our group who was a very original person and interesting and different in many ways, Subhashish Chakraborty with whom we would discuss the lab issues, basketball games and life in general. Aleksandra Tomic, my very good friend and colleague, who has this genuine kindness that I admire so much, Cemil Kayis and Morewell Gasseller, my lab-mates and good friends who were always ready to assist not only with the lab related tusks but any day-to-day life surprises. I wish to every graduate student to have such nice colleagues in the group with whom you may genuinely be honest even if their philosophical views of the world sometimes differ from your own. It was a great pleasure to have these two young men as my coworkers and friends.

I would like also to thanks all my friends in this Department, Post-Docs and graduate students; some of them have already graduated and others that are still working hard on their projects: Mykita Chubynsky, Tatyana Sharpee, Mikael Katkov, Emil Bozin, Mikael Crosser, Mustafa Al-HajDArwish, Ion Mouraru, Mahdokht Behravan, HyunJeong Kim, Chigusa Ohbuchi, Gassem Al-Zouli, Nikoleta Theodoropoulou, Peter Tobias and

other. It was very nice to have these people around, share opinions, professional experience, discuss physics questions or simply cheer each other up occasionally. I wish them all best of luck and great success in their professional carriers.

I should attribute my special thanks to Ms. Debbie Simmons for her constant assistance on different occasions, always ready to give a timely advice or remind of something important that one may forget to do. Her professionalism and responsibility for her work are truly remarkable.

I should thank Dr. Reza Loloee and Dr. Baokang Bi for their help with sputtering and all clean room equipment that I used. I am very thankful to all the stuff members of the machine shop, particularly James Muns, Thomas Hudson, and Thomas Palazzolo for their help and assistance and great sense of humor. The reason I could do such a precise measurement it is because these people are precisely the experts in their work.

I would like to thank my dear friends Dali Giorgobiani and Maria Bailey for their friendship through all the 17 years that we know each other. Dali herself is a PhD graduate of Physics Department; she was the person who suggested I applied for the Graduate school at MSU. I am very thankful for this great opportunity in life. I also would like to thank my old childhood friends Liana and Asmara from Georgia whom I do not see them often but I appreciate very much their friendship and support. I know how much they are happy for me.

Finally, I would like to thank my family: my parents, Giorgi and Tsiala and my sister Irina, whose love and support I feel every day. Lastly and very importantly, I would like to thank my husband Juri who has an extraordinary patience with all things I do in

life including my devotion to my work. He has been supportive and patient with me during all these years, often encouraging me and always believing in me.

Here at MSU Physics Department, I grew up to become a mature and wise person and I hope I am maybe approaching a boundary to become a good scientist. I believe that the horizons in science are unlimited and despite all the great discoveries that were already made we still live in a very young universe where in my view the scientific knowledge has to be a main tool for understanding the nature.

This work was supported by the National Science Foundation grant No DMR03-05461 and the Alfred P. Sloan Foundation. The W. M. Keck Microfabrication Facility provided valuable resources for fabrication and scanning electron microscopy.

TABLE OF CONTENTS

LIST OF TABLES

LIST OF FIGURES

Chapter 1

Introduction

Semiconductor technology has revolutionized solid-state physics and its applications. We use the products of these technological achievements in our every day lives using computers, CD and DVD players, cellular phones, satellite television, and much more. The most advanced semiconductors are based on atomic layer by layer growth using molecular beam epitaxy (MBE); this technique allows the bandgap of the material to be controlled with amazing precision. Using MBE, high-mobility two-dimensional electron systems (2DES) can be created in GaAs and Si crystals. These 2DESs have been a focal point for both theorists and experimentalists, for more than few decades. In addition to technologically important high mobility field-effect transistors, 2DESs have served as fascinating quantum system for the investigation of fundamentals in electron interactions.

A 2DES can be produced at an interface of two distinct layers (called a heterojunction) doped nearby with atoms that donate electrons. At low temperatures the electrons at such a junction are confined to the lowest quantum state in the direction normal to the interface. Biasing the gate electrodes on the top surface of the heterostructure depletes the region below the gate. Similarly, electrons can be further confined in the other directions to make dots, wires, and other shapes.

Many of the experiments on these systems have been what are called transport studies. In these measurements, a current is passed in one direction of the sample, and the voltage both parallel and perpendicular to the current is measured. In the presence of a

magnetic field perpendicular to the 2DES, these experiments have helped discover amazing physics, like the integer quantum hall effect (IQHE) [Prange, von Klitzing, Laughlin 1981] and the fractional quantum hall effect (FQHE) [Tsui, Laughlin 1983], which became one of the most studied many-body phenomena.

Si/SiO_2 and GaAs/AlGaAs are the most common two-dimensional electron system materials that have been studied over the years. While Si/SiO_2 FETs are the most common for electronic devices, GaAs/AlGaAs systems are often more attractive for physics experiments due to their very high mobility. In recent years, many more phenomena like single-electron transport, and conductance quantization in quantum point contacts (QPCs) have led to further technological advancement [Sohn, Kouwenhoven, Schön]. The potential for exploiting these and many other quantum effects is leading to new approaches to logic and quantum information processes. For example, single electron charges and spins can represent bits of data. Quantum information processing is based on the coherent interactions of these "qubits" [Likharev, Bennett, DiVincenzo].

Despite the many experiments already performed on 2DESs and all that builds upon the new science and phenomena made possible by these experiments, researchers have been very curious to image the motion of electrons in 2D plane space, to see how electrons actually move or interact [Topinka]. Obviously many details can be reviled and understood by electron-transport measurements, yet most of the knowledge of electron behavior in 2DEGs is still indirect when it is based on macroscopically averaged quantities. Imaging techniques could be used to further revile the fascinating interplay that occurs in the system on the nanometer scale.

First, the invention of the scanning tunneling microscope (STM) [Binnig 1982,

Binnig, 1999] in the mid-eighties, allowed scientists to directly view the pattern of atoms on a material's surface. But, additional methods are needed to image the charge distribution beneath the surface. The advancement of other scanning techniques in recent years reviled new directions in the study of electron behavior in the confined nanostructures in the heterostructured samples. The examples of those are: the 2D layer, 1D quantum wires, quantum dots QD and even the smallest quantum structure like a single atom embedded inside the semiconductor.

Our interest in imaging the 2DES with scanning techniques was inspired by very exciting theoretical work [Koulakov, Moessner]. This theoretical work predicts, based in Hartree-Fock calculations, the formation of charge density wave like structure (CDW), for the higher Landau level fillings at moderate magnetic fields. According to these predictions the "bubble" or "stripe" phases are ground states of the 2DE system. Electronic transport measurements seem to verify some of these theories, but do not conclusively explain the nature of this interesting phenomenon. Thus, it makes the problem very interesting for studying with a scanning probe.

A second experiment probes the quantum mechanics of semiconductor donor impurities. Atomic scale electronics inside the semiconductor is one of the most popular ideas proposed for the semiconductor-based quantum computer [Kane, Skinner, Golding]. In particular, Kane [1998] and Golding [1999] have proposed quantum computer systems based on the electronic states of defect atoms. Few recent tunneling resonant experiments helped to understand the physics of donor-related tunneling mechanism [Lok, Caro]. With regard to the donor layer study, we shall investigate the possibility of a successful application of our capacitance probe technique to learn about

the quantum states of the isolates donors as well as the interaction between the wave functions of closely spaced dopant ions. Using the tunneling capacitance spectroscopy it could be possible to measure the energy levels of the isolated dopant atom that binds an extra electron to its proximity.

In present work, we shall focus on studying the GaAs/AlGaAs heterostructured samples with a scanning technique called the Charge Accumulation Imaging (CAI) [Tessmer 1998, Levi, Finkelstein]. The next section of this part of this chapter will introduce the physics of 2DES in perpendicular magnetic field, and briefly describe the charge density waves (CDWs) [Koulakov, Moessner, Aliegner, Glazman] theory. This chapter will conclude with a brief introduction to the physics the donor layer system, particularly the Si^{+} δ-layer. More detailed theoretical background along with an experimental findings for the CDWs will be presented in Chapters 5. Chapter 6 will similarly present the theoretical background and experimental study of the donor layer charging in the same sample. Chapter 2 discusses heterostructured samples and how they are grown, it presents a sufficiently detailed discussion of the physics of heterostructures that are essential for understanding many aspects of the physics presented in this work. Chapter 3 mostly covers the details of the technique of CAI and a subsection is devoted to the description of the experimental apparatus. The detailed numerical calculation for CAI spatial resolution will be presented in Chapter 4 [Kuljanishvili]. And finally, Chapter 7 will summarize the experimental efforts and present possible future directions.

1.1 2DES in presence of magnetic field and charge density modulations

The energy quantization of two-dimensional electrons in a perpendicular magnetic field lies at the heart of the integer quantum Hall effect (IQHE). The regular Hall effect for 3D bulk samples was discovered in the 19th century, when Edwin Hall measured a voltage perpendicular to the direction of current flow in a conductor placed in a magnetic field. This Hall voltage increases in proportion to the strength of the magnetic field.

In the 2D case, the classical picture of the electronic motion in a transverse magnetic field is that the electrons move in circles, with the radius called the cyclotron radius R_C that gets tighter with increasing magnetic field B. This means the angular frequency of revolution, called the cyclotron frequency $\omega_c = (eB)/m$ increases with the field, where e is an electron charge and m is an electron mass. In 1980, it was discovered by Klaus von Klitzing and coworkers that the Hall voltage of a 2D electron system is not simply proportional to the applied magnetic field, but rather increases in distinct quantized steps[von Klitzing]. These steps arise from the interplay of discrete quantum states with magnetic field and disorder. These voltages were found to be related to fundamental physical constants: Planck's constant and the electronic charge. Also, where the Hall voltage is quantized, the 2D electrons carry current with no energy dissipation, much like a superconductor does. These phenomena formulate the integer quantum Hall effect for which their discoverers won the Nobel Prize in physics in 1985. A good understanding of the integer quantum Hall effect is possible by considering how electrons carry current when their energies are quantized into Landau levels (LL).

For the ideal two-dimensional system in a magnetic field B the quantum

mechanical problem was solved by Landau [Prange]. In the Landau gauge $A = (0, Bx, 0)$ and the magnetic field pointing in z direction the wave functions of the electron in the x y-plane and the energy spectrum are given by equations (1.1) and (1.2) correspondingly [Davis].

$$\Psi_{Nk}(x,y) \propto H_N\left(\frac{x-x_k}{l}\right)\exp\left[-\frac{(x-x_k)^2}{2l^2}\right]\exp(iky), \qquad (1.1)$$

where N is the energy level index, the H_N is the Hermite polynomial and the parameter ℓ is the magnetic length.

$$E_{Nk} = \left(N+\frac{1}{2}\right)\hbar\omega_c, \text{ for } N=0,1,2... \qquad (1.2)$$

where $\hbar$ Planks constant divided by 2π. These energy levels are called the Landau levels (LL's). The spatial extent of the wave function is of the order of the magnetic length $\ell = (\hbar/eB)^{1/2}$ of electrons. Another important length scale is the cyclotron radius $R_c = V/\omega_c = \ell\sqrt{2N+1}$, where V is the electron velocity. These LLs are equally spaced by an energy given by Planck's constant times the cyclotron frequency $\hbar\omega_c$, and they are labeled N=0, 1, 2, etc. This spectrum is an example of the close analogy between a 2DES in a magnetic field and a one-dimensional harmonic oscillator. Because E_{Nk} is independent of k, for a given N there may be many degenerate states. Similar quantization of electron energy levels occurs in atoms, where an electron's closed orbit also requires its wavelength to be only certain values. However, unlike atomic energy levels which can accommodate only a few electrons each, a single Landau level in a sufficiently large magnetic field may contain hundreds of millions. This degeneracy is given by eB/h, the

number of state per unit area per spin in each LL. At magnetic fields large enough to resolve the LLs under realistic conditions, the electrons within each LL are generally spin-polarized. The degeneracy of each spin-resolved LL allows a 2DES with a density ρ to fill $\nu = \rho h/eB$ total LLs, where ν is called the filling factor. For typical electron densities on the order of 10^{15} m^{-2}, several Tesla are required to force all the electrons in the 2DES into the same lowest LL, where $\nu \leq 1$. The filling factor can be adjusted either by varying the electron density or the magnetic field.

In real samples, however, there is always a disorder, which broadens the delta-function density of states of each LL. In addition, if we have electric field, it causes some of the electrons to drift through the array of impurities. Solving the problem of a 2DES in an in-plane electric and perpendicular magnetic field under the influence of impurity potentials, we find that the degeneracy of LL's is lifted. Moreover, the states within each LL may be classified into two categories. On the tails of the LLs, the states are *localized*; they cannot carry electric current across a sample. In the center of the LLs, the states are *extended*; they can carry current. See Figure 1. The formation of localized and extended states can be understood by modeling the disorder as a smoothly varying potential landscape of hills and valleys within the 2DES. In this background impurity potential landscape electrons are suppose to move. At low temperature each electron trajectory can be drawn as a contour in the landscape. Most of these contours encircle hills or valleys and they do not transfer electrons from one side of the sample to another, they are localized states. A few states in the middle, center of each LL will be extended across the sample. At higher temperature, the electrons have more energy so more states become delocalized and width of extended states increases. The density variations shown in

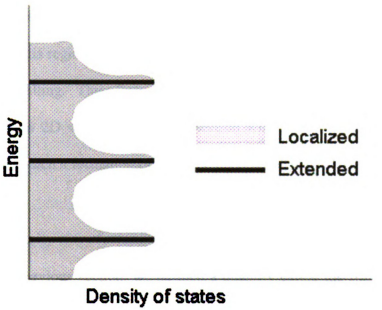

Figure 1. Three LLs broadened by disorder. Extended (conducting) and localized (insulating) states exist in the center and on the flanks of the LLs, respectively.

Figure 1 also lead to compressibility variations. Compressibility is a measure of the energy required to add an electron to the 2DES. Mathematically, we define compressibility as $d\rho/d\mu$, where ρ is the electron density per unit area and μ is the chemical potential. At integer filling, the system is less compressible. Here, the Fermi level is in the region of lower density of states (the dip in the trace in Figure 1, so adding an electron in this region will shift the Fermi level more than if we are at regions further from integer filling. This fact plays a significant role in certain aspects of our measurement on 2D systems. The next section will describe the regime of higher LL occupation in which a formation of CDW states is predicted.

1.2 Charge density wave formation in high Landau levels

In the previous section, we defined a quantity called the filling factor $\nu = \rho h/eB$. The quantum Hall effect is qualitatively different from its classical analog. For 2D systems, the Hall conductance plotted against the reciprocal of the magnetic field shows distinct plateaus at certain values of ν, instead of a straight line. For integer values of ν we have IQHE and in general fractional values indicate FQHE. The FQHE could only be resolved at very high magnetic fields and very low temperatures and $N \leq 2$. At weaker magnetic field regime, or at higher filling factors ($\nu > 4$), the ground state of the system is charge density wave (CDW). Based on Hartree-Fock calculations different groups of theorists independently showed that at higher filling factors a competition between the long-range Coulomb repulsion and the short-range exchange attraction among the electrons in the uppermost partially-filled Landau levels gives rise to a CDW sates [Fogler, Koulakov, Shklovskii and Aliegner, Glazman].

There are two phases called the "bubble" phase and the "stripe" phase. These phases have lower energy then a Laughlin liquid state which describes the FQHE. Calculations show that electrons lower their energy by forming clusters or "bubbles" arranged on a triangular lattice. By adding electrons to the system, the bubbles grow in size, finally to coalesce to form what is called the "stripe" phase [Koulakov, Fogler 1997, Fogler 1996]. This stripe CDW consists of alternating rows of filled and empty states of the uppermost LL. Next the stripe CDW gives way to a triangular bubble CDW solution as the partial filling of the valence LL moves away from one half again. The bubbles and stripes both are separated by $\sim 3R_c$, which is approximately 150 nm for our sample at the relevant magnetic fields.

On the other end, for the few electrons in the uppermost level, the bubbles contain only one electron; this is a type of Wigner crystal. All three phases together are called the charge density wave phase, shown in Figure 2. Our experimental investigation was specifically targeting these ~150-160 nm scale structure. To probe directly for these charge density wave patterns we employ the CAI scanning probe technique.

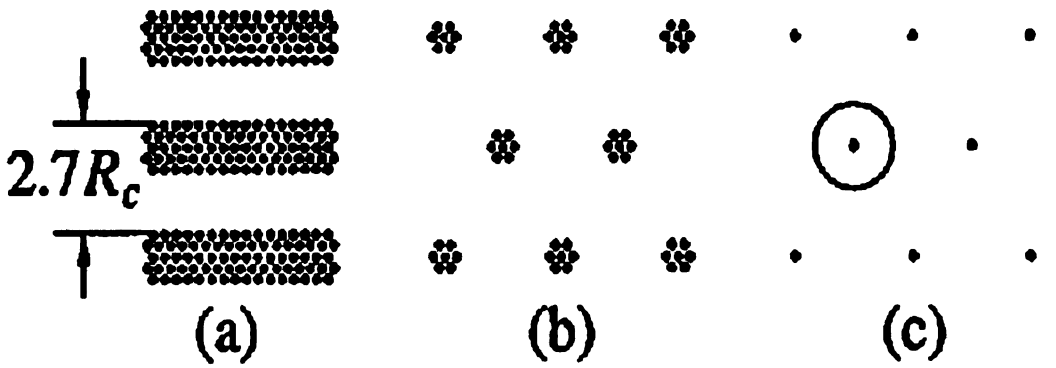

Figure 2. Theoretically predicted CDW patterns [Koulakov]. (a) Stripe pattern. (b) Bubble pattern. (c) Wigner Crystal, showing one cyclotron orbit. The theoretical spacing of $2.7R_C$ between the stripes is at $\nu \approx 4$.

1.3 Donors layer inside the semiconductor heterostructure

Another system that could be conveniently studied using a non-scanning version of our CAI technique is the donor layer of Si atoms that are present in the heterostructured samples. The layer is δ-doped which means that the dopants are confined in an atomically thin layer but randomly distributed within the layer as opposed to bulk doping were dopants are everywhere in the material. More details about the fabrication process will be described in Chapter 2.

Generally, our local probe technique could be considered as a new method for locating and testing the basic properties of individual atoms or donor impurities. A single dopant atom imbedded in a semiconductor crystal represents a smallest possible semiconductor device. At low temperature, in general, the electron or holes can be localized at the parent donor or acceptor. The quantum state of this charge has the potential to be the basic building block of the future quantum computer as noted on page 2 of this chapter. Therefore, the ability to characterize the charge states of the dopant atoms could be extremely important for building functioning semiconductor based quantum computer.

The idea of quantum computing has generated great deal of interest in the research community [Nielsen]. Solid state quantum computing systems are particularly attractive because they allow for the possibility of scaling up the number of quantum bits (qubits) to ~10^5, with the prospect of integration with the state-of-the-art semiconductor device fabrication technology. With regard to candidate systems, qubits constructed from semiconductors such as silicon or gallium-arsenide show considerable promise [Kane, Loss, Smelyansky]. Coherence in quantum state is a very critical issue. So naturally, the

parameter like spin (well isolated from the environment) will provide a long decoherence times for the system but small length scales put limitations on such spin-based qubits. For example, the Kane computer utilizes qubits based on the nuclear spin of phosphorous donors in Si [Kane]. Because of the fact that the exchange attraction between qubits falls of exponentially the separation between donors is required to be 10-20 nm, which represents challenges in process of making the device. An alternative approach makes use of the electronic charge degree of freedom quantum dots or in dopant atoms [Chen, Stieveter]. In this approach, the mechanism for qubit-qubit coupling is the direct Coulomb interaction.

The properties of the dopant atoms in semiconductor could be well described by a hydrogen like model. In gallium arsenide, the corresponding Bohr radius of about 10 nm sets the size of the wave function. This size is much larger than for the hydrogen atom and is due to the scaling for the effective mass of the carriers and the screening effects of the dielectric constant of the semiconductor.

For the sample we probed, the Si donor layer resides 60 nm below the surface of the sample and 20 nm above the 2D conducting layer. We can study the system of the dopant atoms with the capacitance tunneling spectroscopy technique as will be described in details in Chapter 6. This donor assisted tunneling technique can give us chance to study the donor atoms energy spectra, their interactions with each other and the effects of correlation between the electrons and screening effects of the dielectric environment.

Chapter 6 will describe the scanning probe measurements that have been performed on GaAs/AlGaAs sample with Si being a donor atom. We will present the first attempts to study the capacitance spectroscopy of the donor layer inside the

GaAs/AlGaAs heterostructure in the tunneling regime and to locally investigate the energy levels of the dopants atoms and the effects of the proximity of nearby neighbors.

Chapter 2

Heterostructured samples

Semiconductor heterostructures are semiconductor materials that are made of layers with different compositions. Variations in compositions are used to control the motion of electrons and holes through the band engineering [Davis]. In all later discussions, we shall assume few simple approximations. First, we shall use the standard simplification that conduction electrons are free particles with an effective mass. It means that an electron at the interface of the heterostructure can be treated using an elementary problem of a particle in a potential well. Secondly, the random nature of alloys is usually neglected which allows treating them as crystals.

Many III-V materials have been studied for their properties but only a few are eventually used in a heterostructure design. Since the active regions of heterostructure are usually at or very close to the interfaces, they must have nearly perfect interfaces; hence, interface properties are critical in forming a heterostructure. For example, it is essential for materials in adjacent layers to have a similar crystal structure and their lattice constants to be as close as possible. Moreover, surface roughness scattering will compromise the mobility of the electrons. These conditions are met in gallium arsenide, GaAs, and aluminum gallium arsenide AlGaAs (these are not chemical formula but abbreviations). The sample that was use in the studies described in this thesis belongs to this type of heterostructure.

AlGaAs has a wider bandgap than the GaAs, and a slight doping of the AlGaAs layer produces an electric field, essential to bend the bands, forming a quantum well at

the interface; the electrons that are given up by the dopant atoms form the 2DES. Heterostructures should have an atomically sharp interface if they are to perform well. Additionally, the layers are usually very thin and require changing of composition very rapidly during growth. Also, the interface must be contamination free. Hence, it is a challenge to grow such structures. The most common growing technique is the molecular-beam epitaxy, [Davies], with which it is possible to grow highly abrupt junctions between different materials. It also allows atomic scale control over the thickness of layers.

2.1 Molecular-beam epitaxy

Samples used in these studies were grown by the molecular-beam epitaxy technique by Loren Pfeiffer and Ken West at Bell Labs, Lucent Technologies [Pfeiffer, West]. Molecular-beam epitaxy, or MBE, technique is very simple in its essentials. Here we briefly describe the principles of this method.

Figure 3 shows a schematic picture of the MBE growth chamber. The substrate is heated on a holder, which is situated inside an ultra-high vacuum (UHV) chamber with a pressure of about $\sim 5 \times 10^{-11}$ mbar. The elements that compose the heterostructure are vaporized in individual furnaces with orifices directed towards the substrate, but shielded from it by shutters. These furnaces are called the Knudsen cells or K-cells. The reasons for the UHV environment are the following: First, it is important to prevent contamination of the substrate. Secondly and more importantly, low pressure is advantageous for molecular flow without collisions with other molecules. In this regime,

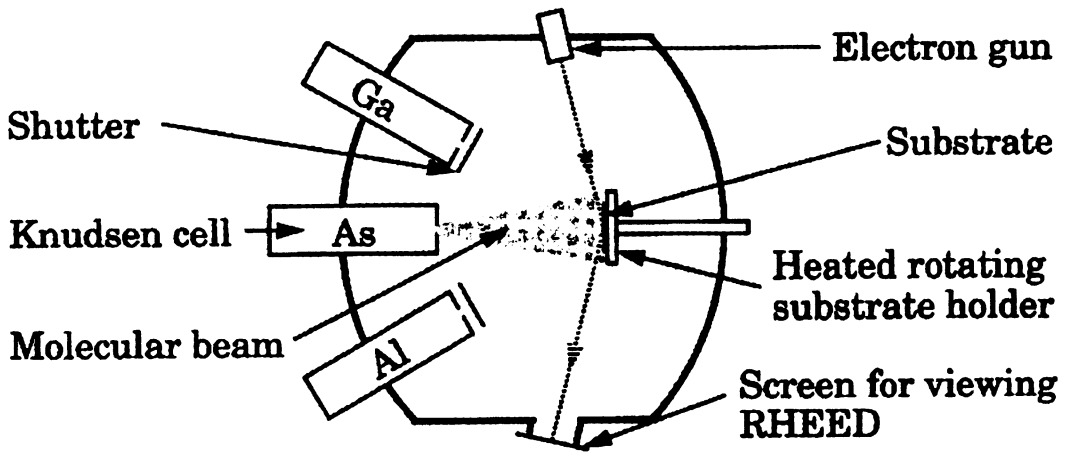

Figure 3. Simplified schematic diagram of an MBE apparatus showing Knudsen cells for Al, As and Ga with shutters. The sample sits on a heated holder, which is rotated during the growth of the sample. The RHEED control system is also shown [Davies].

the mean free path of a molecule is much larger than the length of the chamber, so molecules do not suffers collisions in their path until they meet the substrate [Davis]. This is the Knudsen or molecular-flow regime of gas, and the furnaces are called Knudsen or K-cells. The molecules that emerge from the K-cells do not diffuse as in a gas at higher pressure, but form a molecular beam traveling straight without collisions to impinge on the substrate. Growth starts once the shutters of the K-cells are opened and the temperature of the cells controls the flux of each element. To ensure uniform growth across the substrate, the sample holder is rotated during growth. If dopants need to be added, additional cells are used. A common dopant for III-V systems, such as GaAs is Si. Atoms of Si are group IV in periodic table and could act in principle as donor, or acceptor, in a group III-V compounds. In practice, when grown on (100) surface, Si atoms act as donors, giving up electrons. Our sample is grown with Si by modulation doping, also called remote doping, which will be described in Section 2.3. Moreover, the dopants in our sample are in a "delta" configuration. For δ-doped materials, the dopant layer is very thin, close to a monolayer. We will come back to the discussion of the Si donor layer in our sample in Chapter 6.

Few important steps need to be perfected for ensuring growth of high quality samples. The wafers must be ground with extreme purity, which requires starting materials not to be polluted by the K-cells. The background pressure needs to be kept low to reduce contamination as well as ensure molecular-flow regime. The flux from K-cells must be uniform to minimize the variations in composition across the wafer. The temperature of the furnaces as well as substrate temperature needs to be closely controlled. For example, defects will not have time to be removed by annealing at low

temperatures, while unwanted diffusion will occur and blur the interfaces if temperatures too high.

MBE is a very slow process, and grows material about 1μm per hour. The growth is monitored using one of the common UHV diagnostic techniques called reflected high-energy electron diffraction, or RHEED. With this technique, growth can be counted precisely in monolayers, and it also reveals the structure of the surface. MBE machines of the type shown in Fig. 3 produce very high quality GaAs/AlGaAs samples. The quality of a semiconductor sample is determined by its electron mobility. In the next section we will describe the meaning of this "parameter".

2.2 Electron mobility

Any motion of free carriers in a semiconductor leads to a current. This motion can be caused by an electric field due to an externally applied voltage. This mechanism is usually referred to as carrier drift. Mobility describes the ease with which electrons move in materials in response to an electric field [Ashcroft, Davis]. For completeness, we should mention that in addition, carriers also move from regions of high density to the regions where the density of the carriers is lower. This transport mechanism is called carrier diffusion or thermal diffusion; which is associated with random motion of the carriers. The total current in a semiconductor equals the sum of the drift and the diffusion current. For the rest of this section we will concentrate only on carrier drift.

When electric field is applied to a semiconductor, the electrostatic force causes the carriers to first accelerate. However, they soon reach a constant average velocity, υ, due to collisions with the impurities and lattice vibrations (phonons). The ratio of the

velocity to the applied filed is called the mobility. In absence of an external electric field and considering a large numbers of carriers, the overall net motion of the carriers is zero. When an electric field is applied, there is a net motion along the direction of the field. Let us now analyze the carrier motion considering only the average velocity, υ of the carriers. According to Newton's second law, the acceleration of the carriers is proportional to the total force $\vec{F} = m\vec{a} = m\frac{d\langle\vec{v}\rangle}{dt}$. The net force consists of the sum of the electrostatic force $q\vec{E}$, and the scattering force due to the loss of momentum at the time of collision. The scattering force on average equals the momentum divided by the average time τ between the scattering events (collisions) and has the opposite direction of the electrostatic force. Therefore, the total force is $\vec{F} = q\vec{E} - \frac{m\langle\vec{v}\rangle}{\tau}$. Here q is the charge of the carrier particle. Combining this equation with the Newton's second law, we get the following result:

$$q\vec{E} = m\frac{d\langle\vec{v}\rangle}{dt} + \frac{m\langle\vec{v}\rangle}{\tau}. \qquad (2.1)$$

For the steady state situation where the particle has already accelerated and has reached a constant average velocity, the first term in the right part of the equation (2.1) equals zero. Therefore, the velocity is proportional to the applied electric field and the mobility is defined as the velocity to field ratio.

$$\mu = \frac{|\langle\vec{v}\rangle|}{|\vec{E}|} = \frac{q\tau}{m}. \qquad (2.2)$$

Thus, according to the equation (2.2), the mobility of the carrier in a semiconductor is expected to be large if mass is small and the time between scattering events is large. Lastly, we have to take into account the effect if the periodic potential of the atoms in a semiconductor crystal and use the effective mass m^* rather then a free

particle mass. The unit of mobility is cm^2/ V-sec. All these approximations were made according to the Drude model.

2.3 Formation of 2DES and modulation doping

As mentioned earlier a 2DES is formed at the interface between two semiconductors grown in a UHV chamber under precisely controlled conditions using MBE. In this section, I shall present a brief discussion of the formation of the 2DES in the GaAs/AlGaAs heterostructure with the modulation doping technique [Davies, Prange]. Using MBE, an atomically perfect layer of GaAs is grown, followed by a layer of AlGaAs. The two materials have nearly the same lattice and dielectric constants. Because of the difference in a band gap of the two compounds, the conduction band has a step at the interface. An electric field perpendicular to the interface attracts electrons into a quantum well created by the field and the interface, which will result in an accumulation of the electrons trapped in the quantum well. The electric field perpendicular to the interface is achieved through doping. Let us describe these processes in more details.

The obvious way to introduce the carriers into the semiconductor compound is to dope the regions where electrons or holes are desired. If electrons are needed, the semiconductor compound is doped with n-type material. The question is how to minimize the effects of ionized dopants that are left behind. They can scatter electrons due to the Coulomb interaction and thus spoil the propagation within carefully grown structure. The solution is remote or modulation doping, where the doping is grown in one region but carriers (electrons in our case) migrate to another. This is shown on Figure 4 for a

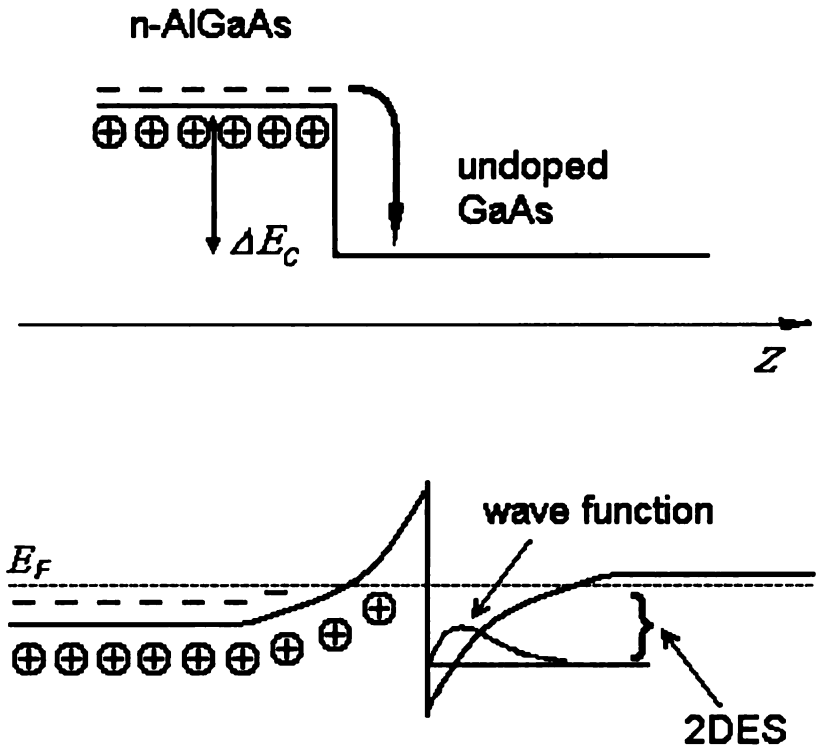

Figure 4. Conduction band around the heterojunction between n-AlGaAs and undoped GaAs showing how electrons are separated from their donors and form 2D electron system. Electrons can diffuse away from the donor ion and some cross into the GaAs. There they lose energy and become trapped because they can not climb the barrier ΔE_c.

heterojunction between n-AlGaAs and undoped GaAs. Here the AlGaAs is deliberately doped n-type, so that it has mobile electrons in its conduction band. GaAs is intrinsically p-type, with few holes in its valence band. The electrons in the conduction band of AlGaAs migrate and eventually fill these holes on the top of the GaAs valence band. However, some electrons usually end in states near the bottom of the GaAs conduction band. The, positive charge left on the donor ions attracts these electrons to the interface and bends the energy band in the process, forming a quantum well. This is the source of the electric field in this system. The transfer of electrons from AlGaAs to GaAs will continue until the Fermi level of the 2DES is aligned with the Fermi level of the AlGaAs. Due to the abrupt step in the conduction band the electric field can only squeeze the electrons against the interface where they are trapped in a roughly triangular well. This well is typically about 10 nm wide at the energy of the electrons, and the energy levels for motion along z direction are quantized similarly to those in a square well. The density of electrons in the quantum well is determined by the dopant density. For sufficiently low doping, only the lowest level is occupied. All electrons then reside in the same state for motion in z direction and move freely in other two directions x and y .This is how 2DES is formed. Figure 5 shows the energy diagram for the resulting quantum well.

An important part of the remote or modulation doping is to place the donors in the AlGaAs physically as far away from the interface as possible. This will further reduce the scattering of electrons in the well by the positive donors and increase the mobility of the 2DES, therefore the refinement was made by leaving a spacer layer of undoped AlGaAs between the n-AlGaAs and GaAs. But there is trade-off: an increased mobility of the 2DES in this case reduces the density of the electrons in the 2D system. Thus, the

optimum spacer thickness depends on the purpose of the heterostructure. For example, high mobility is vital in many physics experiments including present work. On the other hand, for very high performance electronic devices based on heterostructures, it is most valuable to have very high density of electrons in the system; in that case a spacer layer placed between n-AlGaAs and GaAs is extremely thin. A good example for such devices is modulation doped field-effect transistors (MODFETs).

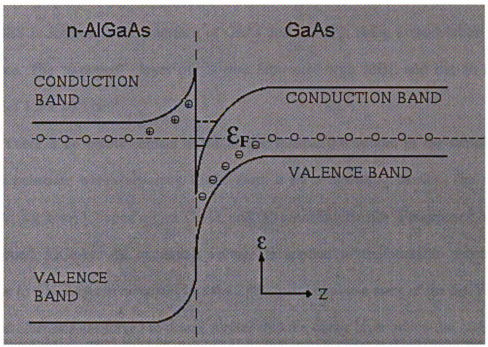

Figure 5. Energy-level diagram of a GaAs/AlGaAs heterostructure. The donor electrons travel from their host Si atom and occupy the first conduction sub-band of the potential well. The Fermi level is shown as ε_F. The spacer layer is not shown [Davis].

2.4 Our sample

The sample and the tip geometry used in our experiments is shown in Figure 6. The sample is a GaAs/AlGaAs heterostructure grown with MBE described in section 2.1. The 2DES is formed at the interface of GaAs and AlGaAs using a modulation doping technique. The "δ-doped" layer of Si was fabricated with MBE and has an averege density of 1.2×10^{12} cm^{-2}.

There is no ohmic contact to the 2DES; instead the bottom of the sample has a metallic substrate which separates 2DES from it by a tunneling barrier. The metallic substrate is a heavily doped n-type GaAs, and the tunneling barrier is composed of layers of undoped AlGaAs. An excitation voltage is applied to the metallic substrate, in response to which electrons tunnel into the 2DES just below the apex of the tip. When tip is biased elecrtons are forced to tunnel further into the donor layer above the 2DES. As a result we have an image charge capacitavely induced on the tip, which is measured. The details of the technique are discussed in the next Chapter 3. The 2DES sits approximately 80 nm below the surface of the sample and 40 nm above the metallic substrate. The mobilty of the sample is 10^5 cm^2/V-sec, and the average density was 2×10^{11} cm^{-2}.

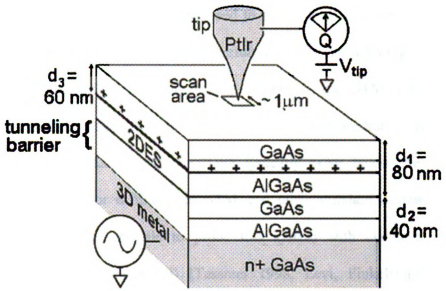

Figure 6. Tip-Sample arrangement of our experiment.

Chapter 3

Experimental set up and the geometry of the technique

Several techniques can be used to image local electronic structure. To examine conducting surfaces, the most powerful technique is scanning tunneling microscopy (STM) [Binnig 1982, Binnig 1999]. However, the STM cannot be used in our experiments because we study electronic systems that are buried inside the sample. The fact that for GaAs/AlGaAs the 2DES typically exists below the surface 40nm-80nm represents a major difficulty to STM and other standard scanned probe techniques. Nevertheless, we are able to probe this system with our technique called charge accumulation imaging (CAI) [Tessmer 1998, Levi, Finkelstein]. The measurement mainly consists of monitoring the induced charging of a sharp metallic tip that is equipped with a charge sensor in response to an ac excitation applied to the sample. The electric field lines emerging from the sample are terminated on the apex of a sharp tip. In this way, charge flowing in and out of the sample capacitatively induces charge to flow in and out of the tip. Therefore, by monitoring this signal, we can locally map out the mobile charges accumulated right under the tip inside the conductive 2D layer. The donor layer situated above the 2DEG, closer to the surface of the sample, could also be studied using this technique.

A detailed description of our technique will be presented in section 3.1 of this chapter. The design of our scanning head is very similar to a standard scanning tunneling microscope. The details of the scanning head and the brief description of the cryostat operation will be presented in sections 3.2 and 3.3 correspondingly.

The essential part of our experimental set up is a cryogenic charge sensor constructed from high electron mobility transistors (HEMTs) [Mimura], which is attached directly to the tip. This circuit description will be presented in section 3.4.

3.1 Charge accumulation imaging

Charge accumulation imaging is basically a measurement of a capacitance signal translated into voltage by a charge amplifier. One can think of the tip-sample combination as two conducting plates of a capacitor. As shown schematically in Fig. 7, as we apply voltage to the sample we immediately induce an image charge on the tip. This charge is detected by a censor circuit, which is directly attached to the metallic tip. Our technique builds upon one that was first developed and implemented by S. H. Tessmer and coworkers [Tessmer 1998] at MIT, with a few significant differences. For instance, one of the most important differences from the earlier experiment is that we do not have a direct ohmic contact to the 2DES. Instead, we use vertical tunneling geometry from a 3D substrate into the 2D layer. For typical samples, the 3D metallic substrate is located about 40 nm below the 2D layer. Fig. 8(a) shows the schematic picture of the 3D-to-2D tunneling arrangement. The advantage of not having an ohmic contact to 2D is that our measurement becomes insensitive to bulk conductivity of the 2DES. This allows us to probe the system even when it is mostly non-conductive. For example, an insulating state results at certain values of magnetic field when the 2DES is close to an integer Landau level filling. In these cases, having the direct contact to the 2D layer would not allow electrons to enter the bulk of the system and subsequently accumulate right beneath the apex of the tip; therefore, our local signal would disappear.

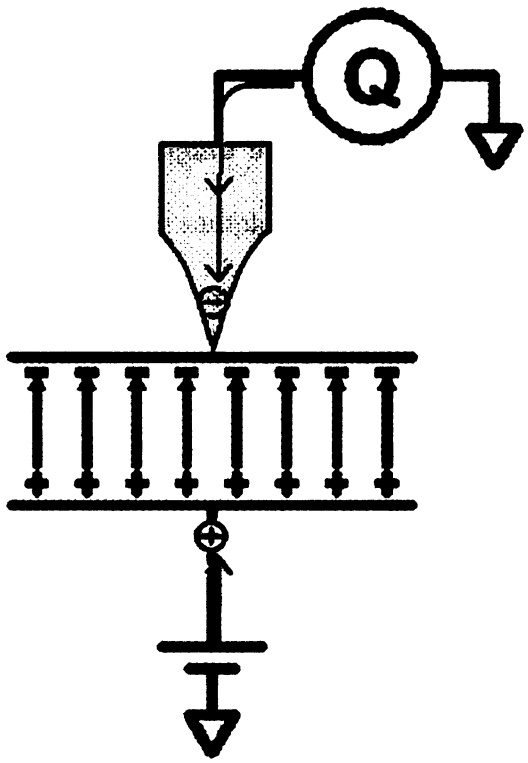

Figure 7. Schematic of the CAI technique. This is a capacitance technique where the tip and the sample are coupled to each other through the electric field, like two plates of a capacitor. To be more specific, we apply voltage to the bottom plate (sample) and monitor the image charge that is induced on top plate (tip).

As shown in Fig. 8(a) our method of measurement with a vertical tunneling geometry does not suffer from this problem. Electrons can enter the 2DES vertically without traveling horizontally through the bulk of the 2DES. We can apply the method in two ways: (1) we can scan the tip to acquire the map-like images of the electron density variations; or (2) while we sweep the sample voltage or magnetic field, the tip could be fixed at a few nanometers away from the surface to acquire a capacitance profile. In addition, our technique is also sensitive to electron correlations which where found to give rise to a so-called Coulomb psuedogap that is pinned to a Fermi level of 2D system [A.H. MacDonald 1997]. This effect can be measured only in tunneling experiments as demonstrated by Ashoori *et al.* [Ashoori 1990] and Eisenstein *et al.* [Eisenstein1992]. Our method can be considered as locally resolved version of those pioneering experiments [Tessmer 1998, Levi, Finkelstein].

All the concepts of our technique that have been described above could also be applied to image the donor layer, above the 2D system. A schematic picture of the arrangement including the donor layer is shown on Fig. 8 (b). The δ-doped Si donor layer is located at 60 nm below the surface of the sample and 20 nm above the above the 2D layer. At sufficiently positive voltages on the tip electrons enter the 2D system and then tunnel further into positively charged Si ions of the donor layer. Thus, we can study the tunneling spectroscopy of the system of donor ions.

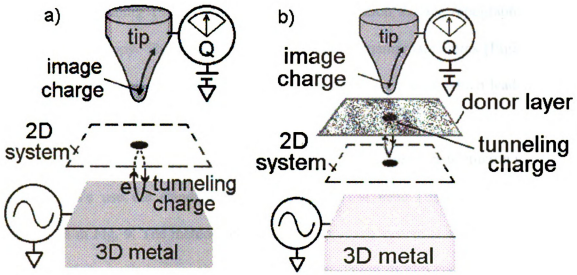

Figure 8. Schematic of the vertical tunneling geometry. (a) In the 3D-to-2D case we probe the charging of the 2DES. (b) In the 2D-to-donor layer case we probe the charging of the donor layer. In both cases an ac excitation is applied to the 3D metallic substrate which resides below the tunneling barrier. The charge tunneling into the 2DES or to the donor layer induces an image charge on the tip, which is measured by a cryogenic charge sensor circuit.

3.2 The scan head

There is a variety of scanning probe microscopes that are used nowadays for studying a wide range of problems. For example, a scanning tunneling microscope (STM) [Binnig 1982, Binnig 1999] can achieve atomic resolution surface topography or high quality spectroscopy. These days STM is also used to manipulate atoms [Eigler, 2000]. Achieving these goals requires very high stability of the scan head, which leads to small piezo lengths and therefore small scan ranges.

The goal of our experiment is to study physics of nanometer-to-micron size range structure. We use the standard Besocke design STM head [Besocke] schematically pictured is in Fig. 9. The method of the kinetic approach system is used here. The main principle of its work lays in so-called inertial translation or slip-stick mechanism. The approach of the sample is achieved by utilizing a sawtooth-shaped or parabola waveform to drive the piezo tube. The waveform of the signal forces carrier-piezo tubes to slowly expand and then quickly contract their length by which they produce the translations in one or more directions. Repeating this hundreds of times allows the sample holding ramps to move with low friction along the slope. This results in the rotation of the ramps clockwise and moves sample in z direction closer to the tip. Similarly, sample can be moved away from the tip when ramps move in the counter clock direction. With the use of the same mechanism sample can be moved in x and y lateral direction for the course positioning purposes. In scanning mode the scanning piezo-tube is moved over the sample in x-y direction. This is achieved by applying voltages to different quadrants of the scanning piezo tube which causes it to bend in x and y direction during the scanning process.

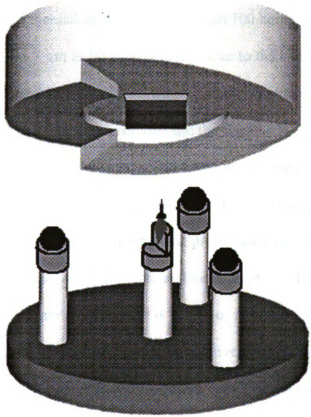

Figure 9. Schematic of the Besocke type scanning head. Three carrier piezo tubes are supporting the sample holder ramps. The sample sits upside-down rigidly mounted on the sample support disk. The outside carrier tubes and the middle scanning tube are all attached to a bottom plate. The scanning tube in the middle holds a small chip with the tip and sensor circuit. (The circuit is not shown.)

In order to increase the scan range of our microscope (scan head) we used very thin 0.125 inch piezo electric tubes that enhance the piezoelectric response. The length of one inch (2.54 cm) was chosen for stability reasons. This design fulfills all our requirements: extreme thermal stability during almost 100 hours of experiment and large scan range up to 7 μm at He3 temperature. Due to the compact design of the scan head, the working area is very small which requires extra caution and adds some challenges while assembling the microscope and the circuit.

The actual picture of the microscope is shown on Figure 10. It has three main stainless steel parts: bottom plate, body and door. The bottom plate holds three carrier piezo-tubes and one scanning piezo-tube. All piezo tubes are made of the same lead-zirconium-titanate material of equal length and outer diameter. The only difference is the scanning piezo tube's inner diameter that is larger, or in other words it has thinner walls. This gives our otherwise short scanning tube relatively large scan range of ~38 μm at room temperature and ~ 7 μm at He3 temperature. Equal length piezo-tubes are important for thermal stability of the microscope, so that they expand and contract identically as the temperature changes. All four piezo tubes are soldered to the bottom plate. Three carrier piezo tubes hold copper feet with stainless steel balls attached to them. The balls are highly polished for low friction performance during the approach of the sample. The center of the scanning piezo-tube has a miniature L-shaped copper cap soldered to it. This copper piece holds the sensor chip with the tip rigidly attached to it. Details of the sensor circuit will be presented later in this chapter in Sec.3.4. Two other stainless steel parts of the microscope are mostly used for the protection purposes and for filling the inside spaces of the probe for maximum liquid He3 displacement. Finally, when all parts are in

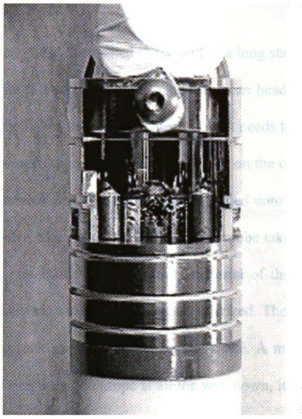

Figure 10. Photograph of the actual microscope. The front door of the microscope is removed and the sample holder ramp is not shown.

place the microscope gets rigidly attached to an eight foot long probe for subsequent lowering of the unit inside the cryostat.

3.3 The Cryostat

Once the scan head is attached to the end of a long stainless steel probe, we place the sensor chip with a cryogenic circuit inside the scan head, mounted on the L shaped copper holder on the top of the scanning piezo tube. It needs to be handled very carefully, because the microscopic sharp tip is already epoxied on the chip. Lastly, the sample gets placed inside the microscope. The probe is then loaded onto the top of the He3 cryostat and is inserted slowly. The process of lowering the probe takes approximately 5-6 hours. It is important to protect the fragile ceramic material of the piezo tubes from thermal stress; the piezo-tubes may brake or become depolarized. The cryostat is equipped with a superconducting magnet surrounding the sample space. A magnetic field up to 10-12 T can be achieved. Once the microscope is all the way down, it is directly in the middle of the magnetic solenoid. Thus, the magnetic field lines inside are lined up exactly perpendicular to the sample. The schematic picture of this arrangement is shown in Figure 11.

The principle of the operation of a He3 cryostat is relatively simple. The whole cryostat is cooled in stages from room temperature to liquid He4 temperature of 4.2 K. First, we cool the cryostat down to 77 K with liquid nitrogen. Then we evacuate the nitrogen liquid and fill the cryostat with liquid He4 (LHe4). The sample space is kept under vacuum during the cool-down procedure. The cryostat can be maintained at liquid He4 temperature of ~4.2 K for months, by filling it up with LHe4 weekly.

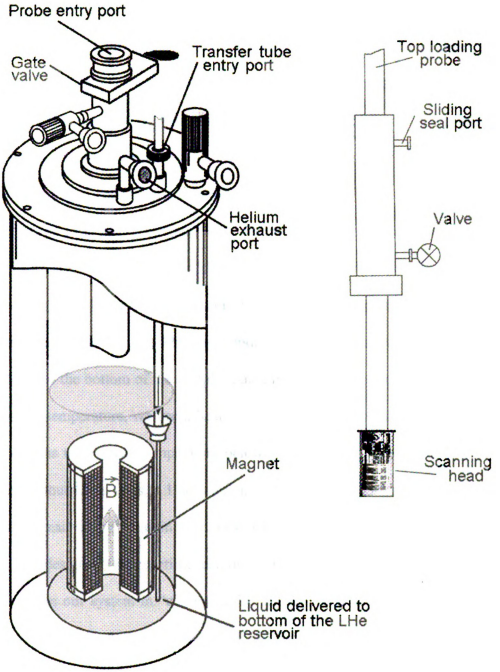

Figure 11. Schematics of the cryostat (left) and top loading probe (right) are shown. During the experiment probe resides inside the cryostat and scanning head is situated at the bottom of the cryostat surrounded by superconducting magnet.

Below I shall describe, briefly, the procedure of the cooling down from 4.2 K to the base temperature of 0.270 K. Outside the sample space and attached to its outer wall is a small chamber called the 1 K pot. First, the 1 K pot is filled with LHe4 and pumped to maintain it at around 1.2 K. The sample space is equipped with a big charcoal adsorption pump, called the sorb.

We assume that He3 gas has been released already from the storage cylinder into the sample space. At this point and sorb temperature is in equilibrium with the surrounding temperature of liquid He 4. As a result, gaseous He3 gets trapped inside the cold massive surface area of the porous sorb. We then start heating the sorb up to 32 K, causing it to release the He3 gas. The He3 condenses onto the cold walls of the 1 K pot and drips down to the bottom of the sample space. In order to avoid overheating the sorb and balance the temperature, we use a heat exchanger which cools the sorb with LHe4. This also helps us to maintain temperature below 1.5 K. The process of condensing the He3 gas takes about 45 minutes to 1 hour. Finally, the base temperature between 0.270 K and 0.290 K is reached by removing the sorb heat; this allows the sorb to pump on the liquid He3. The design of our experiments requires long hours of stable base temperature. Therefore, we run our system in "continues fill" mode where the 1 K pot helium input valve is slightly open for continues flow of LHe4. With practice, the level of opening in the 1 K pot input valve can be adjusted according to its effect on the temperature of the 1 K pot to achieve the lowest base temperature. The sample space remains at the base temperature for about 100 hours, until it runs out of liquid He3. At this point all the He3 molecules are stuck inside the adsorption pump; but they are recycled for next data run.

3.4 The cryogenic charge sensor

There are several types of transistors that could be used for constructing a charge sensor, but most of them are not suitable for our experiments due to incompatibility with low temperatures. For example, bipolar junction transistors (BJTs) depend on thermally activated carriers. These BJTs would be impossible to use because their charge carriers will be frozen out. In general, field effect transistors (FETs) are used for cryogenic applications. However, the power dissipated by such devices is typically in the miliwatt range. This would be large enough to heat up the sample surroundings, shorten the He3 hold time of the experiment, and may cause thermal instability. To overcome these issues we use high-electron mobility transistors (HEMTs). These HEMTs are a kind of field effect transistors that were invented at Fujitsu Laboratories in Japan by Takashi Mimura [Mimura]. These transistors are GaAs/AlGaAs based modulation doped heterostructure devices.

For our charge sensor, the key advantage is the low input capacitance of HEMTs in comparison with the standard FETs, as will be discussed in the following paragraphs. Moreover, these HEMTs can be operated in the ohmic region, far away from saturation. As a result, the power dissipation is decreased by 2-3 orders of magnitude compared to saturation mode operation [Urazhdin, 2002].

Figure 12 shows the schematic picture of the cross section of the HEMT. High electron mobility transistors are fabricated using a heterojunction of a highly Si doped n-type $Al_xGa_{1-x}As$ layer, n-type GaAs and the undoped GaAs. The value of x is representative of a fraction of AlAs in the compound, which is usually 0.3. The epilayers are grown by molecular-beam epitaxy (MBE) on a (100) GaAs substrate. The electrons

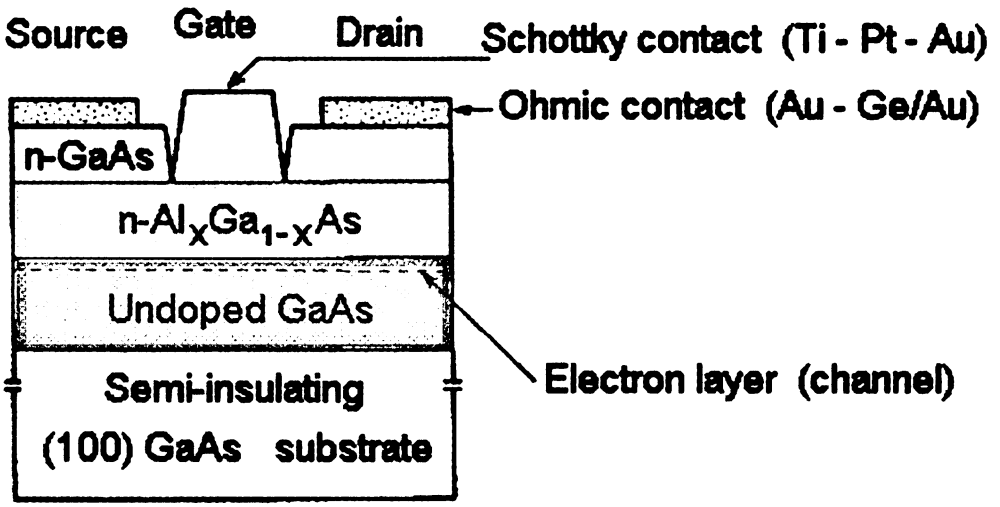

Figure 12. Schematic picture of the cross section of a HEMT [Mimura,1982].

are generated in the n-type AlGaAs drop into the next GaAs layer form a depleted AlGaAs layer. This happens due to the band-gap difference between AlGaAs and GaAs. This results in a steep canyon in the conduction band on the GaAs side where the electrons can move without colliding with the ionized dopants from which they have originated. As you may have noticed already, this is a brief description of how 2D system is usually formed in semiconductor heterostructure. Indeed, in this case the 2D system is the conducting channel of the HEMT.

The schematic of our cryogenic charge sensor circuit is shown in Fig.13.(a). It consists of two HEMTs. The one on the right is the measurement transistor. The gate of the measurement transistor is biased through the HEMT on the left. The role of the bias HEMT is to act as a very high resistor, preventing the charge induced on the tip from leaking to the left. The standard capacitor C_S is used to subtract away the stray (or background) capacitance, arising mostly from the electric fields from the sample which do not terminate on the apex of the tip. This is accomplished by applying an AC, excitation $V_{balance}$ to C_S of the same amplitude but exactly 180^0 out of phase with the applied sample voltage V_{excite}. The typical value of the C_S is about 20 fF (femtoFarad).

To describe our circuit in a little more detailed way let us use a simple model shown in Fig.13.(b). We have already assumed that bias HEMT is tuned to insure the big resistance preventing current from leaking away. We concentrate now on measurement HEMT. The circuit acts like a simple voltage divider. Here V_{in} is the input voltage, in our case V_{excite}, and V_{out} is proportional to the measured voltage V_{meas} / G. Here G is the gain factor. In addition, C_{in} is the input capacitance, in our case it is a capacitance

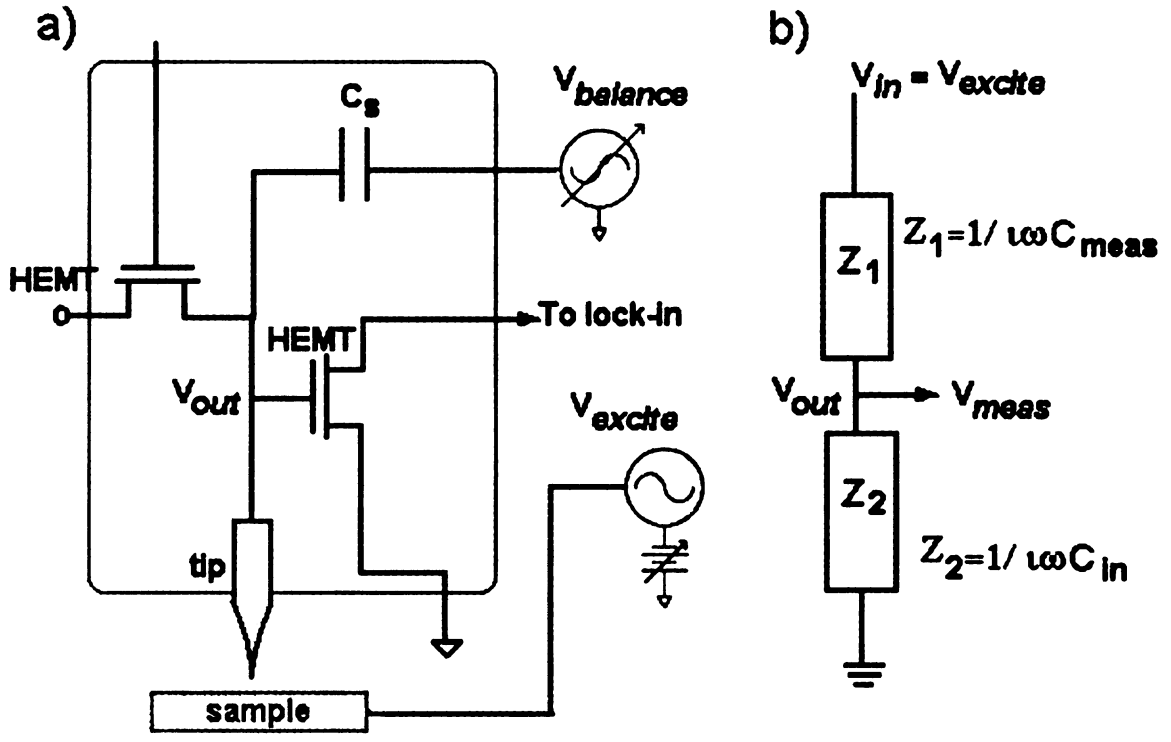

Figure 13. Schematic of the charge sensor circuit. C_S is the standard capacitor and V_{in} is the rms value of the applied AC excitation to the sample. The AC excitation applied to C_S, is of the same amplitude but 180^0 degree out of phase with the excitation voltage that is applied to the sample. The charge sensitivity of the circuit is 0.01 electrons/$\sqrt{Hz}$.

between the gate and the source-drain channel of the HEMT. Lastly, Thus, C_{meas} is the tip-sample capacitance. As it is proportional to the charge, C_{meas} is the quantity that we need to measure. Thus, we can write the following equation:

$$\frac{V_{out}}{V_{in}} = \frac{V_{meas}}{GV_{excit}} = \frac{Z_2}{Z_1 + Z_2},$$

where $Z_1 = \frac{1}{i\omega C_{meas}}$ and $Z_2 = \frac{1}{i\omega C_{in}}$.

Typical value for Z_2 is much smaller than Z_1 therefore we can neglect Z_2 in the denominator of above equation. The voltage measured by the lock-in amplifier V_{meas} is given by the following relationship.

$$V_{meas} = GV_{excit} \frac{C_{meas}}{C_{in}}.$$

Here G is the gain of the circuit, which is usually ~1.The key point, is that low input capacitance means larger signal. The input capacitance of the HEMT is only 0.3 pF. It is important to keep in mind that the stray capacitance adds to this parameter. In other words, the self-capacitance of the entire device must be ~0.1 pF. This sets the 1 mm as the size limit of the circuit.

Our circuit is ultimately limited in sensitivity by the Johnson noise in the bias HEMT which gives a charge sensitivity of 0.01 electrons/√Hz. However, if input capacitance is too large it directly reduces the value of the signal so that other sources of noise will start to dominate, decreasing the sensitivity. The drain current-voltage characteristic curves for different gate voltages of a typical HEMT are shown in Fig.14. We operate our circuit in the low voltage regime far from saturation, indicated by a

circle. Because HEMTs are susceptible to damage from static charge, we check our HEMTs before we even start room temperature testing. Using a device called a curve tracer, we check directly for the characteristic fan-shaped family of curves shown in Figure 14.

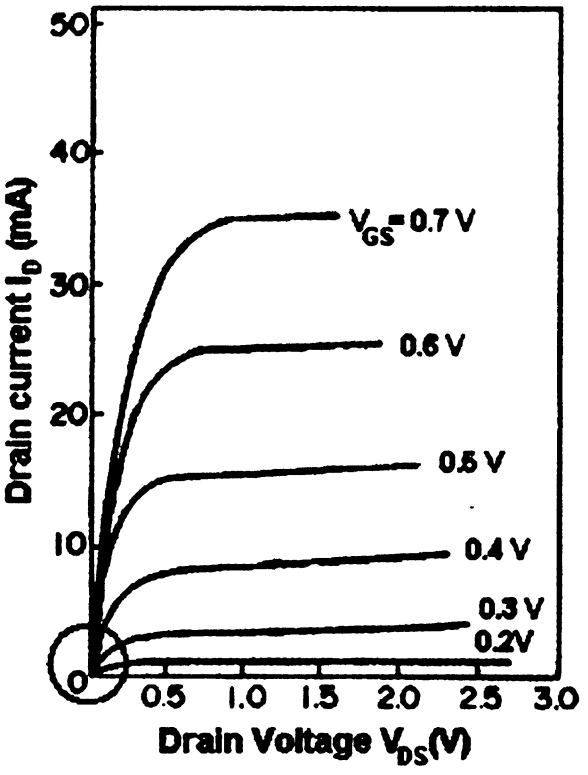

Figure 14. Drain I-V characteristics, at different gate voltages V_{GS}, of a typical HEMT [Mimura,1982]. The circle marks the voltage range in the regime of experimental operation.

Chapter 4

Numerical calculation for CAI spatial resolution.

The tip geometry can be a critical factor for electric-field-sensitive scanning probe microscopies. This is true for techniques such as scanning capacitance microscopy [Martin, Abraham, Huang], scanning single-electron transistor microscopy [Yoo,Yacoby], and charged-probe atomic force microscopy [Erikkson,Topinka], and in addition to our own subsurface charge accumulation imaging technique. The samples of interest typically consist of conducting layers or nanostructures buried beneath a dielectric. To interpret the data and the influence of the tip geometry, researchers often rely on modeling in which the tip is taken to have an ideal shape such as a perfect cone or sphere [Belaidi,1997]. However in many cases the tip may be better described by a less regular shape. For example, the end of the tip may break due to contact with the surface resulting in a truncated cone. Moreover, the tip may be bent or mounted in a non-perpendicular angle so that any model that relies on cylindrical symmetry would be inappropriate. We have developed a straightforward numerical method that can conveniently model a tip of *arbitrary* shape [Kuljanishvili, 2003].

Our method is based on a boundary element approach – inspired by the numerical method used to model the charging patterns within a GaAs-AlGaAs two-dimensional electron layer probed with the CAI technique [Tessmer, 2002]. As shown in Figure 15.(a), we approximate continuous tip and sample electrodes as arrays of point-like conducting elements. By considering the Coulomb interaction among all the elements and using image charges to account exactly for a dielectric overlayer, we directly solve for the complete self-capacitances and mutual capacitance for the tip-sample system.

Here, we introduce the method and demonstrate its utility by calculating the mutual capacitance of a realistic tip and sample used for a CAI measurement. We then compare the resulting modeled spatial resolution to experimental measurement. Below we will describe in details the architecture of our modeling.

4.1 Electrostatic framework

Following basic electrostatics [Jackson], for a system of n conductors each with potential V_i and charge Q_i, the voltage is a linear function of charge:

$$V_i = \sum_{k=1}^{n} A_{ik} Q_k \,, \tag{4.1}$$

where the elements A_{ik} represent a potential matrix $\hat{A}$, and give the voltage of point i due to unit charge at conductor k and all other charges equal to zero. The matrix is symmetric: $A_{ik} = A_{ki}$. In our typical calculations, roughly 25% of the n conductors correspond to tip points and 75% correspond to sample points. Inverting Eq.4.1 yields an expression for the charge on each conductor, which depends highly on the surrounding conductors and dielectric medium:

$$Q_i = \sum_{k=1}^{n} C_{ik} V_k \,,\ \hat{C} = \hat{A}^{-1} \tag{4.2}$$

where the C_{ik} are the coefficients that make up the capacitance matrix $\hat{C}$.

Our scheme follows directly from equations (4.1) and (4.2). We first construct $\hat{A}$ by considering the Coulomb interaction among all pairs of points and invoking image charges to account for bound charges at the dielectric surface, as described below. $\hat{C}$ is then found by inverting $\hat{A}$. The tip-sample mutual capacitance is a quantity of considerable importance for electric-field-based microscopies. Once we have solved for all C_{ik}, we can use Eq. 4.2 to calculate the mutual capacitance. Clearly, the calculation must treat tip points differently from sample points. In constructing $\hat{A}$, three cases arise depending on the identity of each of the pair of points, as detailed in the following subsections.

4.1.a. *Case 1: tip-tip*

Here we consider both i and k to be conductors in the tip. The potential at i due to unit charge at k must also consider the image charge at k' to account for the dielectric, as shown in Fig. 15.(b). In this case the image charge solution [Jackson, New York 1975] is

$$q' = -\left(\frac{\kappa - 1}{\kappa + 1}\right) q ,$$

where κ is the dielectric constant, q is a unit charge located at point k and q' is it's image located at the symmetric position about the vacuum-dielectric interface, k'. The potential matrix element then becomes

$$A_{ik} = \frac{1}{R} - \left(\frac{\kappa - 1}{\kappa + 1}\right)\frac{1}{R'} ,$$

where R and R' are distances from point i to points k and k' respectively.

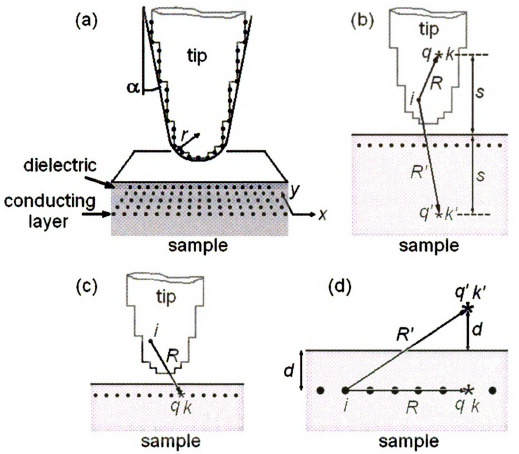

Figure 15. (a) Schematic picture of the finite element approach, showing the tip-sample geometry used to model charge accumulation imaging measurements. The tip is represented by discrete conducting points arranged to form a steep pyramid of half-angle α. The apex is curved with radius r. The sample conductor is represented with points arranged in a two-dimensional square grid imbedded in a dielectric. (b) Schematic of the calculation of potential matrix element A_{ik} for *Case 1*, for which both i and k are points in the tip and k is a distance s from the dielectric surface. The image charge at the symmetric position with respect to the vacuum-dielectric interface k' accounts exactly for the modification in potential due to the dielectric layer. R and R' are the distances from i to k and k', respectively. (c) Schematic for *Case 2*, for which i is in the tip and k in the sample. Here the dielectric layer is accounted for using an image charge at the location of the actual charge. (d) Schematic for *Case 3*, for which for which both i and k are points in the sample a distance d below the dielectric. In analogy to *Case 1*, the dielectric layer is accounted for by invoking an image charge at the symmetric position k'.

4.1.b. Case 2: tip-sample

Similarly we calculate the coefficients of potential for point i in the tip and point k in the sample. In this case, point k is immersed in the dielectric and the image charge solution results in a simple reduction of the potential:

$$A_{ik} = \left(\frac{2}{\kappa + 1}\right)\frac{1}{R} \quad ,$$

where R is the distance between points i and k, as shown in Fig. 15.(c).

4.1.c. Case 3: sample-sample

Lastly, if both i and k are conductors in the sample, the dielectric surface is accounted for with an image charge term analogous to *Case 1*.

$$A_{ik} = \frac{1}{\kappa R} + \frac{1}{\kappa}\left(\frac{\kappa - 1}{\kappa + 1}\right)\frac{1}{R'},$$

where R is the distance from conductor i to k in the sample, and R' is the distance from conductor i to k', located at the symmetric position about the vacuum-dielectric interface, as shown in Fig. 15.(d).

4.2 Results and discussion

4.2.1. CAI measurements

We have employed charge accumulation imaging to study the local structure of the interior of a two-dimensional electron system embedded within a GaAs/AlGaAs heterostructure. For the data we will model here, the sample contained a 2D layer 60 nm

below the exposed surface; the dielectric constant of the overlayer is approximately κ = 12.2. The tip was a chemically-etched PtIr wire with a half angle $\alpha \approx 8°$ for the conical section, and a nominal apex radius of curvature of r = 50 nm [Materials Analytical Services]. Below the 2D layer the sample contained a heavily doped metallic substrate (3D) separated from the 2D layer by a tunneling barrier. As described in detail in Section 4.3, *ac* excitation voltage (20 kHz, 8mV rms) applied to the 3D substrate causes electrons to tunnel from the 3D to the 2D. The charge that enters the 2D layer induces *ac* image charge on the apex of the tip, which is positioned a few nm from the surface. We measure this capacitively induced image charge Q_{tip} using a cryogenic high electron mobility transistor attached directly to the tip.

The local measured charge induced on the tip can be expressed as

$$Q_{tip}(x_0, y_0) = \int \phi(x,y) c_{mut}(x - x_0, y - y_0) dx dy , \quad (4.3)$$

where $\phi(x, y)$ is the effective local ac potential in the 2D layer and $c_{mut}(x, y)$ is the tip-2D mutual capacitance per unit area of the 2D layer [Tessmer,2002]; $c_{mut}(x, y)$ is a crucial function that sets the spatial resolution of the technique. Below we describe the application of our method to calculate this function.

4.2.2. Mutual capacitance calculation

We modeled the tip as a set of point conductors forming a steep pyramid

terminated with a rounded apex, as shown in Fig. 14(a), with $\alpha = 8°$ and $r = 50$ nm. The apex was positioned directly above the center of the sample a distance of 5 nm from the surface. The sample model consisted of a square array of grid points to form the 2D layer, fixed at a position of d=60 nm below a $\kappa = 12.2$ dielectric layer. We used a spacing of 20 nm between adjacent points for both the points that represent the tip and the grid points that form the 2D layer to approximate continuous conductors. Of course, neither the tip nor sample can be infinite in extent; we took the total tip height and sample width to be 0.52 μm and 1.06 μm, respectively. With respect to length scales ~100 nm, these sizes are sufficiently large so that edge effects do not contribute significantly to the charging near the center of the sample and near the tip's apex. The total number of conductors (tip+sample) in the calculation was 3,746.

Here we use a standard programming software, Matlab 6.0 version (Matlab-short for Matrix Laboratory). This software is specifically convenient for manipulations of large matrices. We first solve for $\hat{C}=\hat{A}^{-1}$ and then we find $c_{mut}(x, y)$ by calculating the charge on each grid point of the 2D layer per unit potential difference applied between the tip and sample. This is most conveniently accomplished by considering the tip to be at potential V with the sample grounded. The summation in Eq. (2) then involves only points in the tip. We can further rewrite Eq. 4.2 by dividing each term by voltage and area:

$$c_{mut}(x_i, y_i) = Q_i / (Va) = \sum_{k}^{tip} C_{ik} / a ,$$

where (x_i, y_i) refer to the coordinates of point i in the sample, and a is sample area per grid point.

Figure 16. shows the resulting calculated mutual capacitance function $c_{mut}(x, y)$. We see that it is a bell-shaped function peaked directly below the tip's apex at the center of the sample. The breadth of this peak determines the spatial resolution of the measurement, which we characterize using the half-width at half-maximum, w=92 nm.

To check the errors introduced by the discrete grid spacings and truncated tip and sample, we performed similar calculations using spherically shaped tips with no dielectric layer, and then compared the calculations directly to the analytical solutions. We estimate the plotted $c_{mut}(x, y)$ function is accurate to within 10%, with the exception of points near the edges.

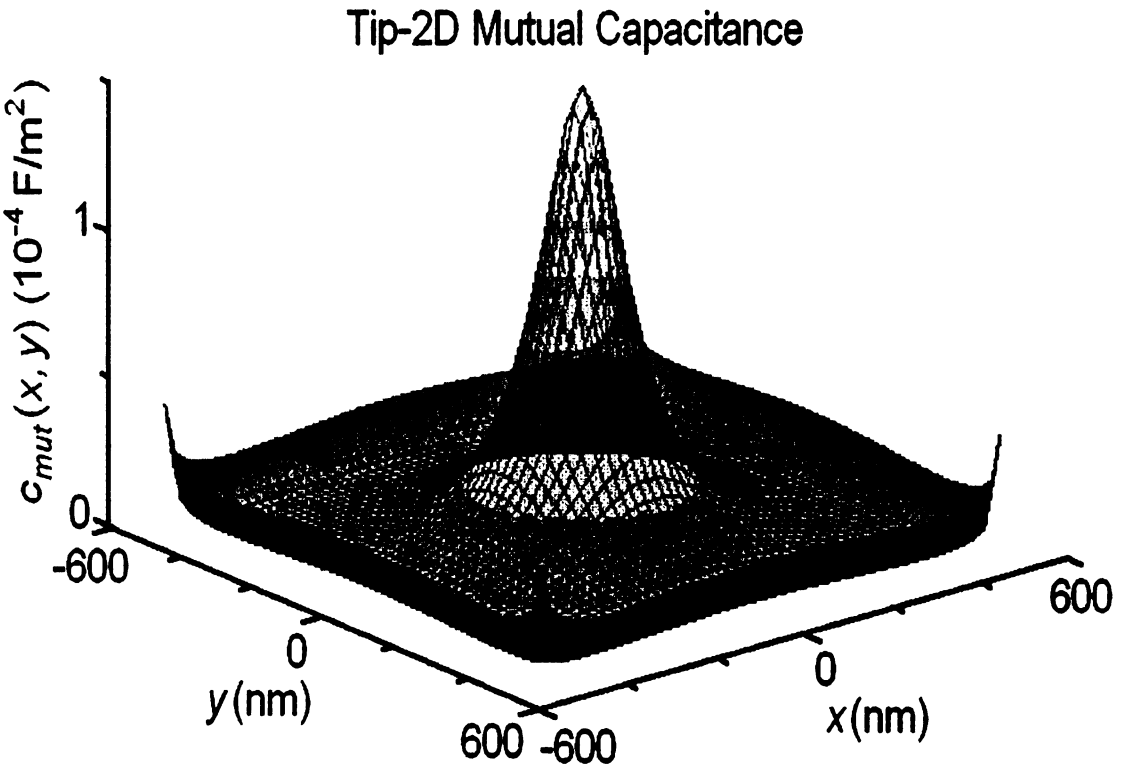

Figure 16. Calculated mutual capacitance function *c(x,y)* showing the characteristic bell shape. The calculation used the tip geometry shown if Fig. 1(a) with a half angle α =8°, radius *r*=50 nm, total height of 520 nm, and tip-surface separation of 5 nm. The modeled sample was 1.06 x 1.06 μm, with a dielectric overlayer of *d*=60 nm. For both the tip and sample the spacing between adjacent grid points was 20 nm. The half width at half maximum is 92 nm, which determines the spatial resolution of our technique.

4.3. Comparison to measured data

To compare these calculations to measured CAI images, it would be instructive to select an image exhibiting an especially sharp feature so that we can assume the true physical extent of the feature is much smaller than w. In that case, the measured width would be mostly determined by the experimental resolution. Figure 17 shows such a comparison. Here, image was acquired by colleagues, Maasilta and Chakraborty, on a sample similar to one studied in this thesis. The measurement was performed at 1° K in a top loading helium-3 cryostat. A depleting voltage of -0.23 V was applied to the tip which serves to significantly enhance the effect of density variations to produce contrast in the measurement. The imaged features simply reflect sample disorder. To calculate the model charging profile we assume that the effective potential $\phi(x, y)$ varies as an arbitrarily sharp step function along the direction of the white line. The step function is smeared out by convolving it with $c_{mut}(x,y)$ following Eq. 4.3. As shown in Fig. 4.3(b), the resulting curve reasonably approximates the experimental spatial resolution with no adjustable parameters.

The common picture for the spatial resolution of electric field sensitive scanning probe measurements holds that the radius of curvature of the tip and the tip-sample conductor separation set the resolution length scale. Because the radius of curvature is the smaller length for our modeled system, we can estimate roughly that the length scale should equal 65 nm, the depth of the 2D layer (d) plus the additional tip to surface distance. This simple estimate is supported by calculations of Eriksson *et al.* based on a numerical routine that solves the Laplace equation in an axially symmetric geometry. For a similar tip-sample system with the tip in direct contact with the dielectric surface, the

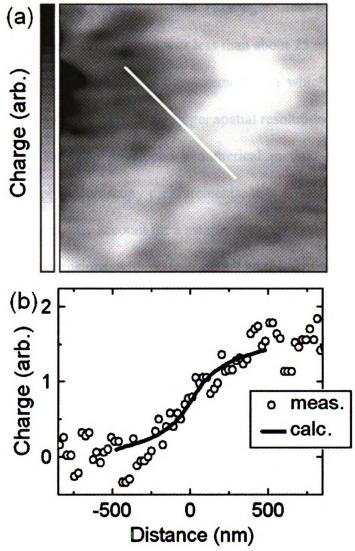

Figure 17. (a) A 3 x 3 μm subsurface charge accumulation image of a GaAs-AlGaAs two-dimensional electron layer formed in a GaAs-AlGaAs heterostructure. The contribution of surface topography has been subtracted so that the displayed signal arises solely from disorder within the two-dimensional layer. The image is filtered to remove nanometer scale noise. For comparison to modeling we focus on the data indicated by the white line; here the signal increases abruptly, representative of the sharpest features imaged by the technique. (b) Cross section of the image along the white line, compared directly to our model calculation as described in the text. In this case no filtering was applied to the measured data, and no adjustable parameters were used in the calculation to achieve the fit.

calculations showed that the half-width at half-maximum of $c_{mut}(x, y)$ was approximately equal to the depth of the 2D layer, $w \approx 1.0d$. (The agreement between w and d was to within 5% as long as the area of contact was less than about 25 nm.) In contrast both our calculation and our experimental CAI measurements, in which the tip is not directly touching the surface, show a significantly larger spatial resolution length scale of $w=1.5d$.

In summary, we have developed a numerical method to model electric field sensitive scanning probe microscopy measurements. It is a finite element approach that uses image charges to exactly account for a sample dielectric overlayer. The elements can be arranged in three dimensions, with no restrictions on the symmetry of the tip geometry -hence it is straightforward to model a tip of arbitrary shape. We have applied method to calculate the expected spatial resolution of a subsurface charge accumulation imaging system. The model predicts a spatial resolution length scale 50% greater than the thickness of the dielectric overlayer, in reasonable agreement with the sharpest features seen in the images.

This calculation showed the resolution of our experimental techniques to be well within 100 nm scale limit. It is an important factor in our measurements. In next two chapters and I will present our main experimental findings and their possible interpretation.

Chapter 5

Charge density waves theory and observations

In this chapter, I will present some background for the charge density wave (CDW) theory based on Hartree-Fock approximation and also show our experimental findings related to the observation of about 200 nm length scale structure that could be related to CDW structure predicted by this theory. Two-dimensional electron systems formed in GaAs/AlGaAs heterostructures represents an ideal environment to study many-particle physics in lower dimensions. Since the discovery of the integer (IQHE) and fractional (FQHE) quantum Hall effects the problem of the ground state of an interacting 2D system is one of the most interesting in the field of condensed matter physics. In presence of the magnetic B field, the system is highly degenerate and Coulomb interaction play a significant role. Depending on various conditions, electron-electron interactions can result in ordered inhomogeneous states. The most extreme example is Wigner crystal (WC) [Fukuyama, Platzman, Anderson]. Certain conditions of course are necessary for the WC formation: low enough temperature, density and disorder. At higher densities though, there is a competition between so called Laughlin liquid state and CDWs.

In the quantum limit, where only one Landau level is occupied ($N \leq 1$), a uniform uncorrelated spin-polarized electron liquid forms a charge density wave structure. This picture is realized only in high magnetic field. It was also later calculated with HF approximation that the optimal period of the CDW coincides with that of the classical

WC but the difference was that electrons were smeared over a distance of the order of magnetic length $l = \hbar/\sqrt{m\omega_c}$ around the sites of the WC [Fukuyama, Yoshioka, Lee].

Let us now consider moderate to week magnetic fields, or in other words high Landau level numbers . In the presence of moderate or week perpendicular magnetic field more general picture arises. Under such conditions the ground state of the electronic system is represented by various phases of CDWs [Koulakov]. The essential assumption in this theory is that Landau levels are still present in such magnetic field ranges. This simply means that even in week magnetic fields, where the cyclotron gap $\hbar\omega_c$ is small the electron-electron interactions do not destroy the Landau quantization.

At higher Landau level filling, Hartree-Fock based theories predict a CDW ground state of length scale on the order of the cyclotron radius, resulting from the competition between Coulomb repulsion and exchange attraction [Koulakov, Moessner]. For typical samples with densities ~10^{11} cm^{-2}, and magnetic fields of ~ 2 T the predicted length scale is ~100-150 nm. Several transport measurements of high-mobility samples show that highly anisotropic behavior occurs for more than four filled spin-split Landau levels, with the uppermost level near half filling [Lilly]. Unidirectional CDW stripes oriented along the [110] crystalline direction are believed to be able to explain these observations. Of course the transport measurements give only an indirect way of testing the spatial structure of the 2D electronic system. Our scanning probe technique indeed provides us with a direct way of studying electronic behavior of 2D system in heterostructure sample by imaging it in real space. Moreover, previous experiments performed in our group, [Maasilta] showed first direct images of an ordered structure within the interior of a GaAs/AlGaAs 2DES. Structures on these images exhibit clear

orientational order roughly along the [110] crystalline direction. The features were suggestive of surprisingly large micron-scale stripe-like states. However, because the spacing between features were a substantial fraction of the experimental scan range, only the approximate value for the characteristic length scale was given without discussion to the periodicity of the structure.

In this chapter, I am going to present only some theoretical details about the formation of the CDWs states and discuss our experimental findings related to a smaller length scale structure of about 150-200 nm. Challenges associated with our measurements will also be discussed in this chapter along with the suggestions for future improvements.

5.1 Description of the theory of CDW

Let us introduce a bit of history on this subject. Prior to 1982, physicists believed that the ground state of the 2DES in a perpendicular magnetic field was described in a form of charge density waves (CDWs). Yet this theory based on HF state picture, failed to explain the FQHE at the time of its discovery. The explanation was made possible when Laughlin [Laughlin 1983] suggested the non-HF state of uniform density for the fractional numbers of $\nu = \frac{1}{3}, \frac{1}{5}, (\nu = \kappa_F^2 l^2$ is a spin-split filling factor), which happened to be lower in energy by a few percent. This was shown rigorously for the lowest Landau levels (N=0,1). However, Laughlin liquid theory does not describe important electron-electron correlations at a partially filled LL. In the years to come in 1990s it became more evident, both from calculations and experiments, that FQHE was likely to be absent for N>1. In 1996, Koulakov, Fogler, and Shklovskii [Koulakov, Fogler 1996] and Moessner

and Chalker [Moessner, Chalker 1997] independently proposed theory alternative to the Laughlin liquid theory of the uniform uncompressible state. Of course one should be clear in that the Laughlin liquid ground state was shown to have lower energy than the conventional Wigner crystal [Wigner] for N >1. However, the Hartree–Fock based theory by Koulakov, Fogler and Shklovskii, predicted that the ground state of various phases of CDWs, in the uppermost Landau levels have lower energies than the Laughlin liquid ground state for N >1. Soon after these theories were introduced transport measurement [Cooper, Lilly] was indirectly suggested the existence of the predicted CDW phases. Here, below we describe the key theoretical arguments that show why the CDW phases are favorable for N >1.

Let us add few more important parameters before we continue further. One more relevant length scale is the classical cyclotron radius R_C given by $k_F\ \ell^2$, where k_F is the Fermi wave vector. Other important parameters are $\nu_N = \nu - 2N$, where ν is the spin-split filling factor, already mentioned above and N is the number of completely filled Landau levels. The factor 2 comes from the spin splitting of the Landau levels. If we follow the calculation assumptions from the calculations of Koulakov, Fogler, Shklovskii work we get this picture.

Assuming that Wigner crystal (WC) [Wigner] is a ground state of the 2DES in a perpendicular magnetic field, one can calculate the cohesive energy of the WC for the case when ν_N is not too small ($\nu_N >> 1/N$), i.e., when the cyclotron orbits at neighboring lattice sites may overlap [AG]. Of course, in the case when ν_N is indeed small, the cyclotron orbits do not overlap, and the concept of WC is natural. Cohesive energy is defined as the energy per particle at the upper Landau level with respect to that in the

uncorrelated electron liquid (UEL) of the same density. The WC cohesive energy for not too small ν_N is given by [Koulakov]

$$E_{coh}^{WC} = -\frac{\hbar\omega_c}{16\pi N}\left[\frac{\sqrt{2}}{r_s} + \frac{3}{2\pi}\ln(N\nu_N)\right] - \frac{1-\nu_N}{2}\hbar\omega_c\frac{\ln(Nr_s)}{2N+1}. \qquad (5.1)$$

The factor r_s is defined by $r_s = \sqrt{2}/k_F a_B$, where a_B is the effective Bohr radius. In realistic samples $r_s \sim 1$. Let us now compare the cohesive energy of the CDW state, in the same regime, i.e., for $\nu_N >> 1/N$. It is given by [Koulakov, Fogler], also see Chakraborty Thesis.

$$E_{coh}^{CDW} \approx -f(\nu_N)r_s\,\hbar\omega_c \ln\left(1+\frac{0.3}{r_s}\right) - \frac{1-\nu_N}{2}\hbar\omega_c\frac{\ln(Nr_s)}{2N+1}. \qquad (5.2)$$

The function $f(\nu_N)$ is proportional to ν_N for $1/N << \nu_N << ½$. The second term in both cases is the same, and one has only to compare the first terms. So in the regime when $\nu_N >> 1/N$, the first term for the CDW case is more negative than the WC case and thus the CDW state has lower energy and wins over the WC state. For the Laughlin liquid state, comparing the cohesive energy with the CDW state, it is not very obvious from the expressions that the CDW state wins over the Laughlin state for N > 1. But the cohesive energies can be calculated numerically. Results are presented in Table 1, below [Fogler, 1997] for $r_s = \sqrt{2}$. From the Table 1 it is easy to see that for $\nu_N = 1/3$ and N = 0 and 1, the Laughlin liquid is lower in energy. On the other hand for N > 1 CDW sate is the winner. The same is true for $\nu_N = 1/5$ and N > 2.

So, it has been predicted theoretically that CDW states for higher Landau levels (N >1) are preferred, let us try to understand the physics intuitively. As it was mentioned earlier in the Chapter 1 that there is a competition between the long-range Coulomb

$\nu_N=1/3$					
N	$\tilde{M}$	E^{UEL}	E^{L}_{coh}	E^{CDW}_{coh}	$\delta E/E^{CDW}_{coh}$
0	1	−0.1206	−0.1159(1)	−0.1037	−11.8%
1	1	−0.1297	−0.1519(3)	−0.1424	−6.7%
2	2	−0.1136	−0.1141(3)	−0.1188	4.0%
3	3	−0.1034	−0.0946(3)	−0.1018	7.1%
4	4	−0.0965	−0.0824(3)	−0.0896	8.0%
5	5	−0.0914	−0.0733(3)	−0.0805	8.9%

$\nu_N=1/5$					
N	$\tilde{M}$	E^{UEL}	E^{L}_{coh}	E^{CDW}_{coh}	$\delta E/E^{CDW}_{coh}$
0	1	−0.0560	−0.0903(2)	−0.0880	−2.6%
1	1	−0.0765	−0.1727(7)	−0.1692	−2.1%
2	1	−0.0677	−0.1420(9)	−0.1396	−1.7%
3	2	−0.0618	−0.1139(9)	−0.1202	5.2%
4	2	−0.0577	−0.0963(9)	−0.1050	8.3%
5	3	−0.0547	−0.0849(9)	−0.0946	10.3%

Table1. The cohesive energies of the Laughlin liquid E^{L}_{coh} and the CDW E^{CDW}_{coh} for $r_s = \sqrt{2}$. $\tilde{M}$ is the optimal number of electrons per CDW bubble given approximately by $3\nu_N N$. The energy unit is $\hbar\omega_c$. The energy per electron in the uniform uncorrelated state E^{UEL} is also provided for reference [Fogler 1997].

repulsion and short-range ($\sim \ell$) exchange attraction between the electrons, which leads to the formation of clusters of electrons, called "bubbles" and "stripes" with a periodicity of $\sim 3R_C$. But this does not answer the question of why there is no CDW for low Landau level filling (N=0 and 1). The answer on this question is related to the length scale R_c the cyclotron radius, which appears in the exponent of the CDW wavefunction. The wavefunction of a single bubble with M electrons at the lowest Landau level is given by

$$\Psi_0\{r_k\} = \prod_{i<j}(z_i - z_j) \times \exp\left(-\sum_{i=1}^{M} k_F \frac{|z_i|^2}{4R_C}\right). \tag{5.3}$$

Here $z_j = x_j + iy_j$ is the complex coordinate of the *jth* electron. The wavefunction of a bubble at the Nth Landau level centered at R can be constructed from the above wavefunction as

$$\Psi\{r_k\} = \prod_{i=1}^{M} \frac{\left(a_i^+\right)^N}{\sqrt{N!}} \exp\left(\frac{b_i^+ \overline{R} - b_i R}{\ell\sqrt{2}}\right) \Psi_0\{r_k\}, \tag{5.4}$$

where $a_i^\dagger$ is the inter-ladder operator, raising the *ith* electron to the next Landau level, and $b_i^\dagger$ is the intra-ladder operator. Finally, the wavefunction of the CDW, with an anti-symmetric combination of bubbles centered at the triangular lattice sites R_l is given by,

$$\Psi_{CDW} = \sum_P \mathrm{sgn}(P) \prod_l \Psi_l\{P(r_k)\}. \tag{5.5}$$

P's are the permutations of electrons between bubbles. The intuitive reason for the absence of CDW for low Landau level fillings (N =0 and 1) is as follows [Fogler Koulakov, also see S.Chakraborty thesis]. In all these arguments we are talking only about electrons in the upper partially filled Landau level. Laughlin liquid can be thought of as a CDW state melted by zero point vibrations. The melting can occur only if the

amplitude of the zero point vibrations is comparable to the lattice constant. This amplitude never exceeds the magnetic length-ℓ. There is an important difference between low and high Landau level filling. At low Landau level filling, Coulomb repulsion dominates, and the electrons can lower their energy by staying as far apart as possible. Hence the CDW contains only one electron per unit cell. The lattice constant is of the order of R_C, and it is small at low Landau level filling, since R_C is inversely proportional to the field. The lattice constant decreases with increasing filling factor, since now the system accommodates more electrons in the same amount of space. At some value of ν_N, the lattice constant becomes of the order of ℓ, the spatial extent of the electron wavefunction in a perpendicular magnetic field, and the crystal melts into a Laughlin liquid. At higher Landau level filling though, increasing the filling factor, adds more electrons to the lattice sites of the CDW crystal, so that the lattice constant does not change much. The lattice constant, which is of the order of R_C, is much greater than ℓ, at higher Landau level filling. Therefore, it is unlikely that at higher Landau level filling the CDW would be melted by the zero point fluctuations.

The CDW state in equation (5.5) forms patterns shown in Figure 18(a) and (b). Each black dot in the figure represents the guiding center of the cyclotron orbits. An enlarged view of a "bubble" is shown in Figure 18(c). The dark region is the guiding centers of the cyclotron orbits of the electrons in the bubble, while the toroid is the charge density distribution. The aggregation of many particles into large domains helps the system achieve a lower value of the exchange energy, while the Coulomb repulsion keeps the aggregates separate. The actual charge density variation of the uppermost Landau level is of the order of 20%. At higher Landau level filling, when the system is very close

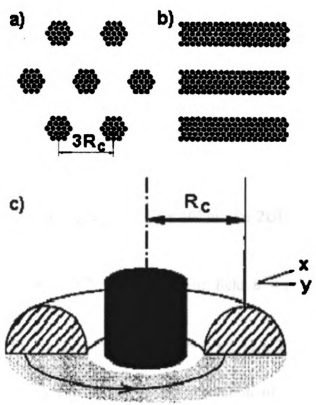

Figure 18. (a) "Bubbles". (b) "Stripes". The black dots are the guiding centers of the cyclotron orbits. The periodicity is ~ 3 R_C. (c) The enlarged quasi-classical image of a single bubble. The dark region is the guiding center of cyclotron orbits and the toroid is the charge density distribution, which is created by electrons moving in the cyclotron orbits centered inside the bubble. [Fogler 1997, Fogler 1996, Chakraborty thesis].

to integer filling ($\nu_N \sim 1/N$), each bubble consists of one electron. As we move away from integer filling more electrons are added to the lattice sites forming the bubbles. This happens as long as $\nu_N < 0.3$. As the system moves further from integer filling, the bubbles merge together to form the stripes.

The motivation for this experiment is to resolve these predicted bubbles and stripes. We have calculated the periodicity of these CDW structures, for the magnetic field we use and the density of our sample. The periodicity of a CDW lattice according to prediction $\approx 3R_c$. Simple calculation shows:

$R_C = k_F \ell^2$, and k_F in 2D = $\sqrt{2\pi\rho}$ = 1.12 x 10^8 m^{-1} for 2DES density ρ = 2 x 10^{15} m^{-2}.

While $\ell^2 = \frac{\hbar}{eB}$ = 3.3 x 10^{-16} m^2 for magnetic field $B \approx 2$ T, which corresponds to ν between 4 and 6 for our sample. Hence $3R_C$ = 3 x 1.12 x 3.30 x 10^{-8} m $\approx$ 110 nm, (for $\nu = 4$) and it is comparable to our spatial resolution of ~92 nm. (See Chapter 4). Similarly one can estimate the length scale for $\nu = 6.5$ which is approximately 150 nm.

In the following parts of this chapter I will present our observation on the charge density variations near $\nu = 6.5$ in a presence of perpendicular magnetic field. And I will also discuss the magnetocapacitance data with the tip fixed at a few nanometers distance to the sample.

5.2 Magnetocapacitance measurement and charge density variations

In this section, I will describe two types of measurements that were performed on a heterostructured sample. First, I shall discuss a magnetocapacitance measurement that was performed with the tip fixed at a constant distance above the sample without scanning. I will then describe our scanning measurements. The charge is driven into the 2DES by an *AC* excitation applied to the 3D substrate. Capacitive coupling between the 2DES and the probe allows us to detect charge accumulated in the 2DES. The CAI technique has been proven to be very successful in imaging local compressibility features in 2DES [Tessmer, Finkelstein] and ordered micron scale features [Maasilta] in an integer quantum Hall regime. Here I will show our attempt to image smaller scaled structure in a similar regime. The essentials of the measurement were already described briefly in Chapter 2 of this thesis. More detailed picture of the measurement is as follows.

Our sample, as already stated before, has a 3D metallic substrate which we use for our ohmic contacts. Thermal diffusion of indium from the back of the sample makes direct contact to a 3D bottom substrate. A tunneling barrier separates the 2D layer and a parallel 3D layer. The standard 2DES is formed at $Al_{0.3}$ $Ga_{0.7}As$ / GaAs interface 80nm below the sample surface. As already discussed before in Chapter 2, our (001) wafer is grown by molecular beam epitaxy (MBE). It has an electron density of $\approx 2\times10^{11}$ cm^{-2} and low temperature mobility $\mu \sim 10^6 cm^2/V$ sec. At zero magnetic field 3D-2D tunneling rate is approximately 200 kHz. This value is extrapolated from the analysis on a similar sample. An *AC* excitation voltage applied between the substrate and a sharp metal tip locally induces charge to tunnel back and forth between the 3D and 2D layers. The surface Schottky barrier blocks the charge from tunneling directly onto the tip. The

resulting measured signal is the *AC* image charge on the tip electrode, which is proportional to the number of electric field lines terminating on it. In this way, the experiment provides a local measurement of the ability of the 2D system to accommodate additional electrons. Our observation show clear evidence of the quantum Hall behavior in the 2DES system. Characteristic dips in the capacitance signal are observed every time system enters the incompressible state. Our observations also show evidence of charge density variations in 150-200 nm scale range. We believe that these are hints of dynamic and unstable CDW type structure.

Let us start by describing the recipe for performing these measurements. All our measurements are performed at cryogenic temperatures that are achieved by direct immersion of whole microscope in liquid He-3, typically at 270 mK. Chemically etched PtIr tip of ~50nm radius is typically positioned within a few nanometers of the sample surface. Positioning of the tip is first achieved in "tunneling mode" regime, where constant tip sample distance is controlled by tunneling current feedback loop. This way tip is positioned at a distance of a few angstroms above the sample surface in "tunneling mode", after which the feedback is switched off. Figure 19 shows the schematic of different modes of operation of our microscope. Usually, the tip is pulled away from sample about 30-40 nm and moved laterally sufficiently far from the tunneling location to unperturbed location. After that, the tip is brought closer to the surface using manual fine approach and left at a fixed distance of 3-4 nm above the surface. The image charge signal is detected on the tip using a sensor circuit discussed in detail in Chapter 3. Most of the signal (~99.8%) corresponds to electric field emanating from areas macroscopically far from the location under the probe. Normally, this background signal

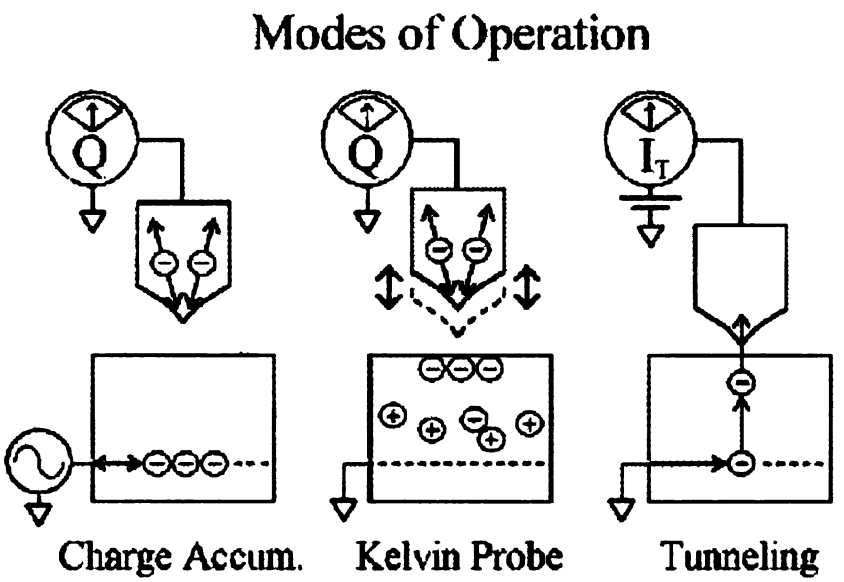

Figure 19. Three modes of operation of the microscope: tunneling mode (right), Kelvin probe (middle) and charge accumulation (left).

gets subtracted away using a bridge circuit. To acquire images of the interior of the 2DES, the tip is scanned laterally across the surface without the use of feedback loop.

Let's concentrate now on fixed tip measurements in the presence of a perpendicular magnetic field. We apply and excitation voltage of 4 mV rms at a frequency f=20 kHz. In addition, we apply a *DC* voltage of 0.6 V to the tip to compensate for the tip-sample contact potential [Tessmer 1998, Yoo] to ensure the effective zero *DC* voltage. To determine this compensating voltage, we perform Kelvin probe measurements, where we mechanically vibrate the tip in the vertical direction with a small 2 kHz frequency and amplitude of ~2 to 4 nm. We then measure the oscillating charge induced on the tip in response to the charge oscillations in the sample. This charge results from the electrostatic potential difference ΔV between the metallic probe and the GaAs sample. It is proportional to ΔV (dC/dz), where C is the probe sample capacitance and z is their separation. We measure the capacitance signal vs *DC* voltage between probe and the sample. We repeat this measurement at different distances between tip and sample ΔZ and from these measurements we deduce the nulling voltage (V_{null}) necessary to compensate the electric field created by the work function difference between tip and the sample (tip-sample contact potential).

Magnetocapacitance data is shown in Figure 20. Here, we plot the measured charging as a function of magnetic field with the tip position fixed. The plot on this figure exhibits clear structure with $1/B$ periodicity if plotted against inverse magnetic field, corresponding to integer Landau level fillings. Usually, two components of the signal are detected for fixed tip data and for scanning images. One is in phase with the applied excitation and the other 90^0 out of phase with it. We call the in-phase capacitance signal

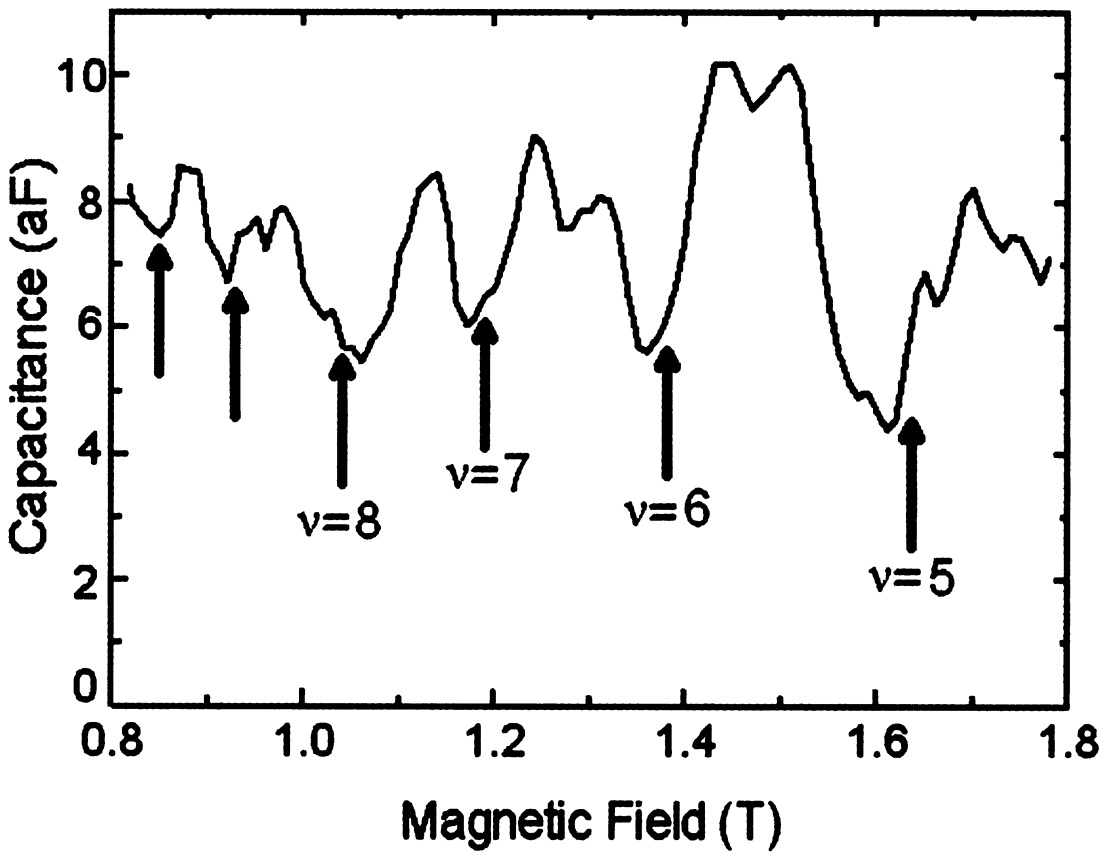

Figure 20. Fixed-tip measurement. Present plot shows measured charging as a function of perpendicular magnetic field with tip fixed at a few nm above the surface. Clear features at integer Landau level filling ν are marked with arrows. (Here only the in-phase component is shown).

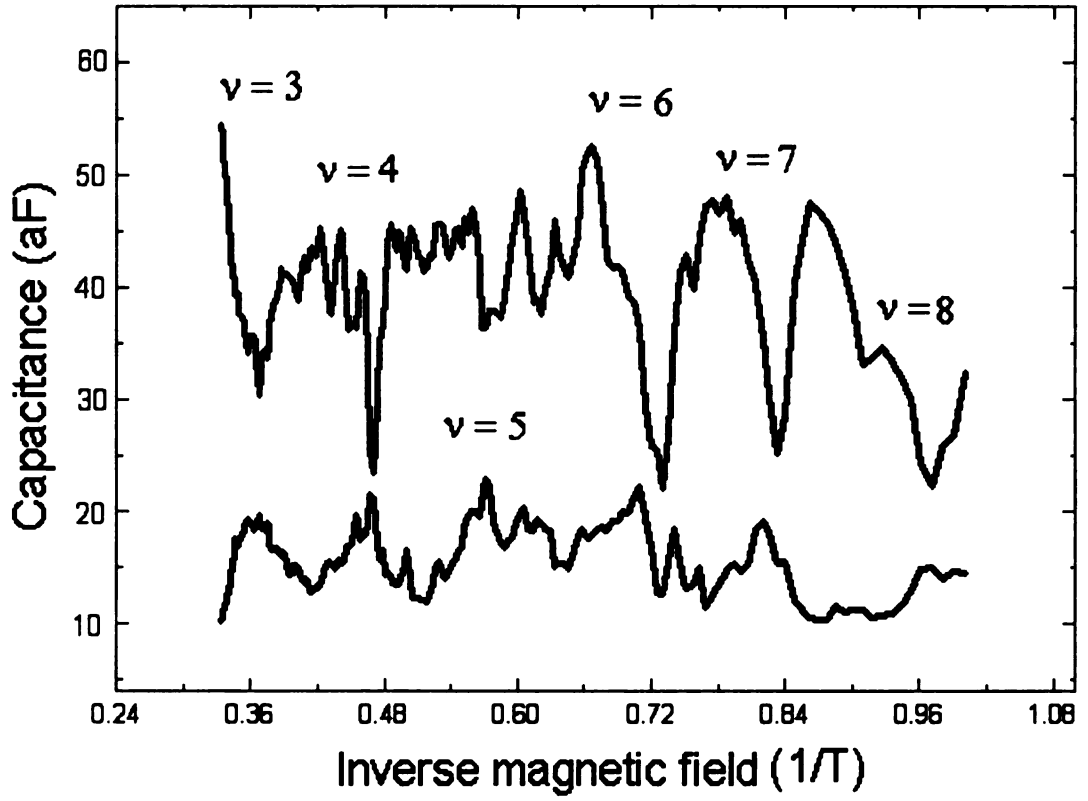

Figure 21. Two components of the signal plotted against inverse magnetic field. Different set of data also taken with fixed tip similar to the measurement shown on Figure 20. In-phase capacitance signal (top curve) and out-of-phase capacitance (bottom curve). Dips in the in-phase curve and much smaller peaks in out-of-phase curve are marked my numbers corresponding to integer LLs.

Q_{in}, and the out-of-phase signal Q_{out}. In Figure 20, we show only the in-phase component of the signal and the dips are representative of the usual behavior of the 2DES as it passes through the incompressible states at integer Landau level (LL) filling. The out-of-phase component usually resembles peaks at the corresponding integer LL fillings. Figure 21 shows similar magnetocapacitance data from a different data set that has both components of the signal plotted with respect to inverse magnetic field. In order to explain the nature of the in-phase dips and out-of-phase peaks, we present the charging characteristics of the model equivalent circuit. Figure 22(a) shows the actual tip-sample geometry and the equivalent circuit. For simplicity, the capacitance between the tip and 2DES is considered as a parallel plate capacitor C_{tip}. Similarly, the capacitance between the 2DES and the metallic substrate is assumed to be another parallel plate capacitor C_T, which is in parallel to the tunneling resistance R_T. These form an RC circuit. The plot of Q_{in} and Q_{out} with respect to the logarithm of the applied frequency f or the tunneling resistance R_T is shown in Figure 22(b).The charging components have identical functional dependence on f and R_T, with characteristic values of $f_0 = [2\pi R_T (C_T+Ctip)]^{-1}$ and $R_0 = [2\pi f(C_T+Ctip)]^{-1}$, respectively. The magnitude of the curves is set by the tip-sample capacitance difference ΔC between a fully charging and locally non-charging 2DES. For the actual measurements, the characteristic zero magnetic field tunneling rate is f_0~200 kHz, a factor of ten greater than the applied excitation (i.e., f/f_0 ~0.1).

If we focus on the model's low-frequency behavior, $f/f_0 << 1$, the out-of-phase component is more sensitive to variations in the local tunneling resistance. In contrast, the in-phase component is mostly sensitive to capacitance variations, including the compressibility contribution to the capacitance [Tessmer 2002, Smith]. In a parallel plate

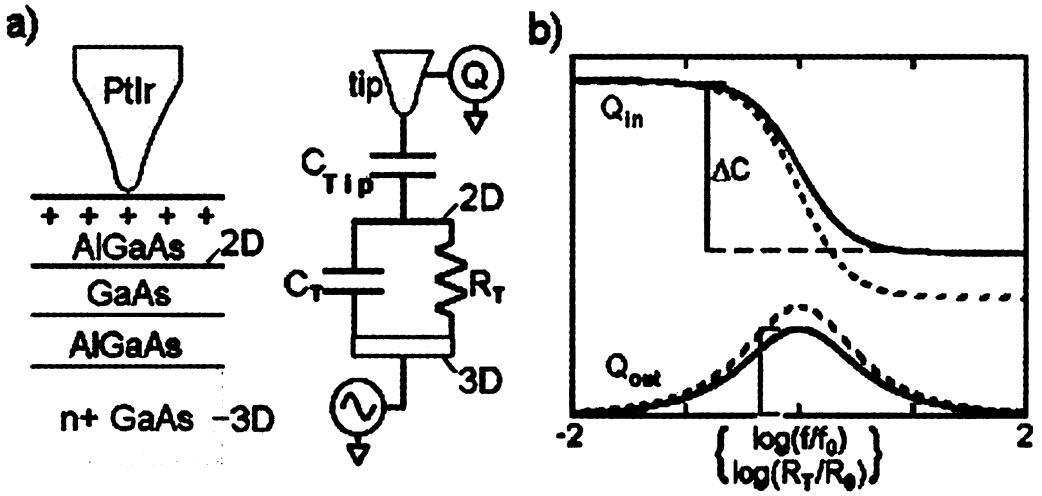

Figure 22.(a) The circuit equivalent to the tip sample arrangement in the 3D-to-2D charging case. (b) Calculated in-phase and out-of-phase charging based on the equivalent circuit. Rigorous modeling for the system considers the distributed nature of the tip-sample capacitance and the effect of charge motion within the 2D plane. The dashed curves show qualitatively enhancements, which occur if the in-plane relaxation rates approach the tunneling rate, an effect that may occur near integer filling [Maasilta ,2003].

capacitor model, the measured capacitance is given by following equation [Stern, Smith].

$$\frac{1}{C_{meas}} = \frac{1}{C_{geom}} + \frac{1}{e^2 \, dn/d\mu} \tag{5.6}$$

where C_{meas} is the measured capacitance and C_{geom} is the geometric capacitance; $\frac{dn}{d\mu}$ is the density of states with respect to the chemical potential. This quantity is often referred to as the compressibility. Thus, one could conclude that the dips in the measured in-phase curve reflect a reduction in capacitance caused by the diminished compressibility of the 2D system at integer filling. With respect to the out-of-phase charging curves (not shown), the peaks that usually appear at corresponding integer filling likely reflect an increase of the pseudo gap, resulting in an increased tunneling resistance R_T [Deviatov].

Let us now move to the charging images. Figure 23 shows a series id the out-of-phase charging images between fully filled and exactly half-filled upper LL, namely between $\nu = 6$ and $\nu = 6.5$. The in-phase component of the signal, (not shown), is typically dominated by geometric capacitance signal and does not reflect the local density variations. These images were acquired on an undisturbed area with tip scanned very close, about 4-5 nm, from the surface. The scan range of ~750 nm was chosen in order to search for the predicted ~110 to150 nm periodic density variations near half-integer fillings.

In this data set we start at the magnetic field values corresponding to the integer filling $\nu=6$. Charging images were acquired at six different values of magnetic field that

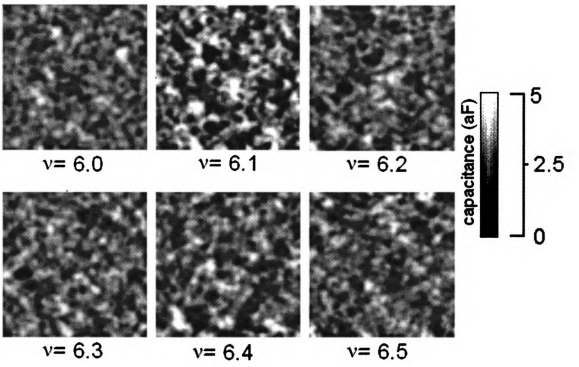

Figure 23. Images of the out-of-phase charging signal are shown. Scan range for all images is identical and equal to 730×730 nm. Images are acquired at ν=6, 6.1, 6.2, 6.3, 6.4 and 6.5 with corresponding B=1.38 T, 1.36 T, 1.34 T, 1.32 T, 1.30T and 1.28 T. The images are filtered to remove the nanometer-scale scatter. The 5 aF contrast indicates ~7 % variation in density.

correspond to incrementing the filling factor by 0.1. We expect to observe the local charge density variations by their coupling to the out-of-phase component of the signal. as demonstrated by Maasilta and coworkers. This density variation occurs due to the variation of the R_T parameter as the system gets closer of further from integer filling. Although it is difficult to see from the direct images, as we approach the half integer filling $\nu = 6.5$, the charging pattern becomes somewhat structured. Figure 24 shows the same set of images (upper row) with their corresponding Fourier transform (bottom row). The bright peaks in the transform indicated ordered structure in the diagonal direction for the image for ν=6.5.

The comparison of the charging image for ν=6.5 and the topographic image of the same location at zero magnetic field is shown on Figure 25. The larger scale image of surface topography is also shown on this figure, which was acquired at room temperature without alternating the sample orientation. The $[\bar{1}10]$ direction is indicated. Hence we see that the orientational preference in the charging images is about 35 degree with the [110] crystalline direction which is often referred to as the "easy direction" for current transport [Lilly, Cooper]. It was suggested by Cooper and coworkers however that at temperatures higher then 150 mK the anisotropic behavior in electronic transport was largely suppressed. Thus, it is believed that the fragments of the CDW structure do not preserve their preferential orientation and thus are more likely to be isotropic.

It must be emphasized, however, that we consider these data as evidence for the charge density variations but not a firm observation of CDWs. Similar quality charging images were not acquired near $\nu = 4.5$. Moreover, we did not see any evidence of a

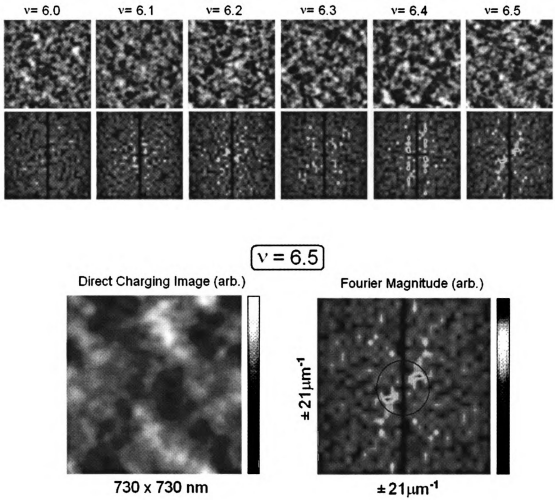

Figure 24. Direct images vs. two-dimensional Fourier transform. Top two rows represent the out-of-phase images in progression from ν=6 to ν=6.5.with their corresponding 2D Fourier transforms (FT) (same set of data as in Fig. 5.3.) Bottom row: enlargement of ν=6.5 direct image (left) with additional filtering and it's FT (right). The circle indicate the wavelength of about 160 nm predicted by theory for our sample. Peaks on this FT image indicate the length of approximately 200 nm future in corresponding direct image (left).

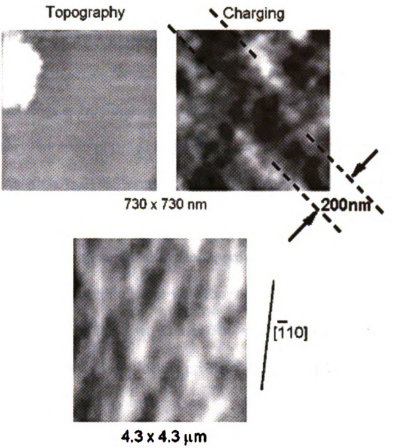

Figure 25. Topography vs. charging image. 730 x 730 nm scan images of topography (left) and out of-phase charging image (right) are shown on the top. Both images are acquired at exact same location. Charging image shows a stripe like structure of ~ 200 nm. Left upper corner of the topographic image shows some surface defect absorbate that does not contribute to capacitances; the rest of the topographic image looks featureless. Larger 4.3 μm image of the surface topography is also shown (bottom); typical growth features of the GaAs surface of ~ 1μm long and ~ 5 nm in height are shown. The black bar indicates the [$\bar{1}$ 10] crystalline direction.

"bubble"- like phase near the integer filling during our experiment. Only a stripe like orientational tendency near $\nu = 6.5$ filling was observed. The length scale of this structure is in relatively good agreement with the predictions of the charge density wave picture. Estimated length scales for our sample is about 110-150 nm. The length scale of the observed structure is approximately 200 nm.

In summary, we have obtained images suggesting an ordered structure within the interior of a GaAs/AlGaAs 2DES using a novel scanning capacitance imaging technique At magnetic fields near six and a half filled Landau levels, we observe density modulations that exhibit orientational order, approximated in 35 degree to the [110] crystalline direction. The structure is not very robust and, therefore, does not allow us to conclude with the certainty about its nature. The structure is suggestive of the high-Landau-level charge density wave structure predicted by theory [Koulakov].

Chapter 6

SPM study of the donor layer charging in a GaAs heterostructure

In this chapter the donor layer charging in a GaAs heterostructured sample will be discussed. As was already described in previous chapters, the 2D system in our sample is formed with a use of the δ-doping technique, with Si being used as the dopant atom. This allows for the creation of monolayer wide sheet of Si^+ ions randomly distributed above the 2D layer. The density of these Si atoms is 1.25 x10^{12} cm^{-2}. One can study the effects of charging inside the δ-doped layer by allowing electrons to tunnel into it from a 2D reservoir. This tunneling will happen when a sufficiently positive voltage is applied to a top gate, or in our case, an effective positive voltage to the tip. This way, electrons fill up the energy levels available in the donor system which is made of the ionized Si.

The basic model for an isolated ionized donor in a semiconductor considers the system as hydrogen ion [Davis]. The mass of the electron is rescaled to the effective mass of the electrons in the host material, and the charge is screened by a dielectric constant of the host. Both effects reduce the ionization energy R substantially from the 13.6 eV for real hydrogen to only about 5 meV for the donors in GaAs and AlGaAs. R called the Rydberg energy, which can be written as follows:

$$R = \left(\frac{e^2}{4\pi\varepsilon}\right)^2 \frac{m}{2\hbar^2} = \frac{\hbar^2}{2ma_B^2} = \frac{1}{2}\frac{e^2}{4\pi a_B \varepsilon}, \tag{6.1}$$

$$a_B = \frac{4\pi\hbar^2\varepsilon}{me^2}, \tag{6.2}$$

Here a_B is the Bohr radius, which is scaled up to about 10 nm for electrons in GaAs and AlGaAs, compared to a_B = 0.053 nm for real hydrogen. To describe the binding of an electron to an isolated donor ion, to a good approximation we can use the textbook hydrogen atom solutions. Thus for the hydrogenic model, the wave function for the lowest state has an exponential form for 3D case [Davis].

$$\Psi(R) = (\pi a_B^3)^{-1/2} \exp(-R/a_B). \qquad (6.3)$$

The Rydberg energy and Bohr radius are defined by equations (6.1) and (6.2), and the energy states are $\varepsilon_n = -R/n^2$. The schematic picture of the wave function for the hydrogenic atom is shown on Figure 26.

Can these hydrogenic ions bind a second electron? For many systems the answer is yes. The state is known as the D^-; these D^- centers are produced by attachment of an extra electron to a neutral donor D^0. These states could play an important role in testing and understanding many-body phenomenon; this subject has attracted a significant interest for many decades since the beginning of quantum mechanics. The behavior of the D^- has been well characterized for well isolated (weakly doped) systems in confined geometry and strong magnetic field. In addition to several optics experiments [Huant, Holmes, Shi], experiments using the resonant tunneling spectroscopy method have observed the D^- states in double barrier resonant tunneling device (RTD) [Lok, Geim].

As the resonant tunneling experiments motivated this part of my thesis work, it is worthwhile to describe briefly the RTD measurements. The idea behind the resonant tunneling is this: the sample is biased and the current flows when the energy of an electron in two-dimensional electron system formed at the interface is resonant with the states in the quantum well. See schematic of this arrangement on Figure 27. As a bias

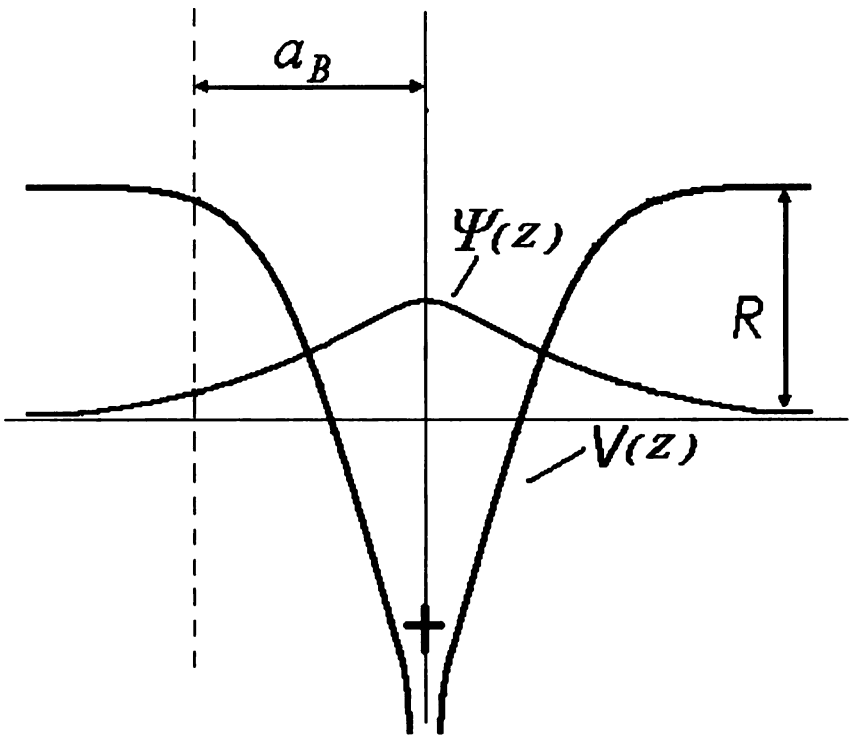

Figure 26. Schematic of the hydrogenic dopant atom. Wave function ψ(z) and the potential V(z) are shown. R is the Rydberg energy and a_B is the Bohr radius.

DC voltage is increased the energy levels in the well pass through the resonant conditions and are showing up as peaks in the *I(V)* characteristics. These, resonant tunneling experiments will be described in more details in section 6.1. The results from our capacitance measurements and the attempts to explain our observations will be described in section 6.2.

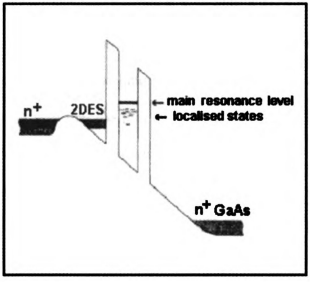

Figure 27. Schematic diagram of the conduction-band profile of the RTD under the bias. Tunneling occurs from 2DES through the ground state in the quantum well (for the main resonance) or highly localized impurity levels at lower energies (Geim 1994).

6.1 Resonant tunneling experiments

The heterostructure interface between AlGaAs/GaAs represents a simple example of the tunneling barrier, similar to one shown on Figure 27. As we know classically, an electron would not be able to pass through the barrier unless it has sufficient kinetic energy to pass over the top, but quantum mechanically it is able to tunnel through the barrier. The opposite of the barrier is a quantum well, for example a relatively thin layer of the GaAs sandwiched between two thick layers of AlGaAs. In this important case where GaAs is surrounded by AlGaAs the electrons reside in bound states and the energy levels can be measured by optical techniques. As we know well from quantum mechanics if we make a quantum well that has thin barriers on both sides, then the electron in the state is not truly bound anymore but *quasi-bound* or *resonant.* There is not a true bound state because the electron can tunnel through and escape from the well. But if the walls of the well are thick enough then electron can remain in the well a long time in a resonant quasi-bound state.

In resonant tunneling experiments [Lock, Geim], the resonant tunneling structure was constructed inside the AlGaAs double barrier with intentional Si δ doping in the quantum well. The thickness of both barriers and AlGaAs was 5.7 nm and the width of the quantum well 9 nm. The structure was fabricated in square mesas of sides of length varying from 5-100 μm and there was a 20 nm undoped spacer layer between the barriers and the doped contact regions. The average donor separation was between 0.1 and 0.5 μm for different samples; this is sufficient so that the dopant atoms could be considered as isolated. But because there is always some statistical probability of finding some of the donors at distances much smaller then average the binding energies of the This is an

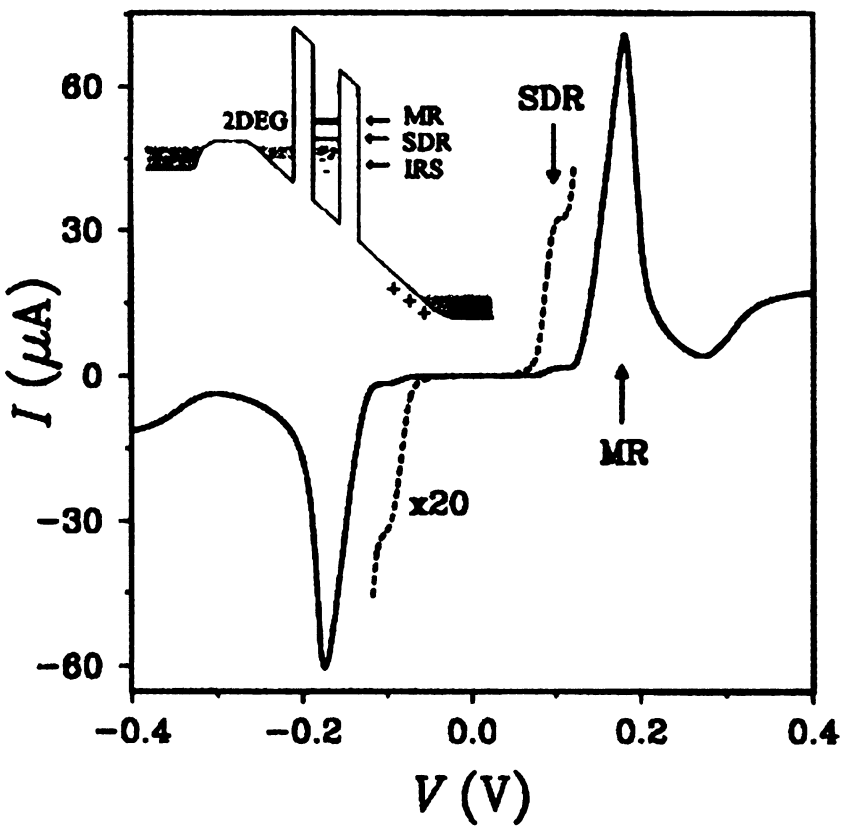

Figure 28. I(V) for the resonant tunneling structure 12 μm across with the δ doping in the well at 1.3 K. The arrows indicate the main resonance (MR) and single donor resonance (SDR). The dashed curve represents 20x magnification of the SDR. The inset shows the schematics of the band diagram for the double barrier tunneling structure. Impurity related states (IRS) also shown on the diagram not visible on the plot. This plot is reproduced from reference [Geim].

interesting aspect of the work described by these groups [Geim, Lok]. Tunneling through the paired donors could become dominant when other states remain out of resonance. The structure and *I(V)* plot for the device with $8x10^9$ cm^{-2} donor concentration is shown on Figure 28. Tunneling occurs when a state in quantum well comes in resonance with the 2DES formed in an accumulation layer near the emitter barrier as the bias is increased showing as the main resonance peak (MR) in *I(V)* plot. The lowest 2D subband in the well gives rise to the main resonance and the δ doping gives rise to an additional resonance at smaller biases which originates form tunneling through the localized ground state (D^0) of shallow donors. There is also additional peak observed in high magnetic field indicating the tunneling through D^- states [Lok].

The RTD observation of D^- centers has a few important aspects to it.Tunneling spectroscopy gives directly the binding energy of the donor state. In addition, the shallow donors in this and other similar experiment have been found to give rise to resonant features described as "donor molecule" levels and donor state coupled with random potential fluctuations, which are not visible on the plot. However, such states were observed at biases below the threshold for the main resonance a broad peak, as shown in Fig. 28. The authors model the observation of deeper levels as being caused by a pair of Si donors situated in a close proximity by random chance; the two dopants are modeled as a simple hydrogenic donor molecule, which we will refer to as "H_2". Binding energies were estimated for a donor pair separated by one Bohr radius and for a triangle of three shallow donors [Geim]. As separation decreases the binding energy increases; in the limit of zero separation it reaches the expected values for Z^2R, where Z is number of donors in a cluster and R is the Rydberg energy. This approach will become relevant for our own

capacitance tunneling spectroscopy experiments, which will be described in the next section.

6.2. Scanning probe capacitance tunneling spectroscopy measurements

In this section, we will describe the new scanning probe approach to study quantum states of the donor atom inside the semiconductor. The concept of the measurement is almost identical to one already described in Chapter 3. The imaging technique will be applied to probe the behavior of the Si dopant atoms in the δ layer of AlGaAs/GaAs sample. Here we will present our first tunneling capacitance measurements that study the system of the quantum states of the donor layer and effects of the proximity to neighboring atoms. This new approach has indeed proved to be a powerful tool for study such systems.

Let's repeat the basic idea of the measurement. With the probe being immersed in liquid helium-3 at a temperature of 270-280 mK we position the tip few nanometers from the surface of the sample. As was already described, the essential part of the measurement consists of monitoring the tip's AC charging in response to an AC excitation voltage V_{excite} applied between the metallic substrate and the tip. By adjusting the bias voltage applied to the tip we can find the potentials for which the dopant energy levels are in resonance with the chemical potential of the substrate. So, generally speaking, at these voltages the electron is forced to tunnel locally on and off between the substrate and the dopants below the tip. Figure 29 shows the schematic of the measurement set up and the conduction band diagram of our sample, including the Si^+ in AlGaAs/GaAs heterostructure as described in Chapter 5.

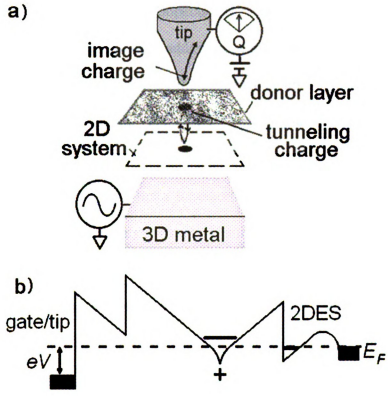

Figure 29. (a) Schematic of the measurement for the study of the donor layer. (b) Schematic of the conduction band of the system.

An accepted picture for a single isolated dopant ion inside a semiconductor at low temperature is a hydrogen ion, as described earlier in this chapter. In samples with the relatively high average density of dopants this picture is incomplete. Moreover, as shown in tunneling resonant experiments, additional features besides the main resonance and D^- and D^0 states could be explained by the existence of other impurity related states. In our measurement we investigate the physics of similar effect with the capacitance spectroscopy technique.

Before describing the main measurements, we show a more basic capacitance measurement performed by my colleague Cemil Kayis on a sample from the same wafer. Instead of a tip, the gate electrode fabricated onto the surface plays a role of the probe. This is an illuminating test because it is very similar to the scanning probe measurement. It has the additional advantages of well-defined parallel plate geometry, and a precisely known measurement area, defined by the 5.7×10^{-7} m^2 area of the gold gate. The result is shown in Fig. 30(a). At sufficiently negative gate voltage, the 2D layer itself is depleted of electrons; hence the capacitance signal corresponds to the gate-substrate separation, which is relatively low. As the gate voltage increases to about -0.5 V, the 2DES becomes populated with electrons. Hence, the two plate effectively get closer together and the capacitance increases. At still higher voltages, the capacitance rises steeply. Here the electrons are entering another layer – the cap layer formed at the GaAs-AlGaAs interface near the gate electrode.

Apparently, there are no clear features due to electrons entering the dopants below the gate electrode. The micron-size area probed in gated measurements such as this have a disadvantage of probing a relatively large area. The vast number of dopants and

impurities below the gate likely allow relatively rare defects to dominate the measurement – effectively shorting out the measurement of the donor layer structure.

We now turn to our CAI technique to probe locally the voltage range where we expect to see evidence of donor layer charging. In order to probe the characteristics of the delta-doped layer we use the similar approach to the one that was already described in Chapter 5 for the magnetocapacitance data. We situate the tip in a close proximity to the sample in capacitance mode. This means we fix the tip at few nanometers from the surface of the sample without the feedback response. In this experiment, we use the presence of the 2D layer below the donor layer as a reservoir of free electrons. Electrons can be induced to tunnel from the 2D into the donor layer when the bias voltage is being swept positive. In the actual measurement we apply negative *DC* voltage to our sample which creates an effective positive voltage in the tip. We monitor the capacitance signal as a function of bias voltage and tunneling events are manifested as peaks in a capacitance signal.

It is important to realize that the effective voltage applied by the tip is scaled-down compared to the gated capacitance measurement in Figure 30(a). The relevant voltage is the 2DES-to-donor layer potential difference. This is proportional to the tip voltage or gate voltage. The proportionality constants are often called the lever-arm factor and denoted as α. The two constants relevant for Figure 30 are $\alpha_{tip} = C_{tip}/(C_{tip}+C_{2D})$ and $\alpha_{gate} = C_{gate}/(C_{gate}+C_{2D})$, where C_{tip} is the tip-to-dopant layer capacitance per unit area, C_{gate} is the gate-to-dopant layer capacitance per unit area, and C_{2D} is the dopant layer-to-2DES capacitance per unit area. For the gated measurement, the capacitances are well defined and give $\alpha_{gate} = ¼$. For the scanned probe

measurements, C_{tip} is small compared to C_{gate}, as the tip is never in full contact with the surface. Hence, we expect α_{tip} to be less than ¼ and the effective voltage to be scaled down considerably. To estimate C_{tip} we have performed detailed numeric calculations, as described in Chapter 4. [Kuljanishvili, 2004]. These calculations, together with calculations performed by Eriksson et al., imply $\alpha_{tip} \approx 1/15$. Lastly, it should be emphasized that we find that α_{tip} changes by as much as 30% when comparing measurements acquired at different locations. This is likely due to variations in the tip-surface separation.

The results of the CAI measurement are shown in Figure 30(b) for which the tip position was fixed (not scanned). Three clear peaks are present as a function of voltage, labeled as A, B and C. Similar peaks were observed in all locations we probed that exhibited a stable signal. To improve the signal to noise ratio, the data shown in the figure represent the average of more than a two hundred hours of data acquisition, sampled at three different locations. (All the data shown in subsequent plots were acquired at a single location.)

Are these peaks related to the D^0 and D^- states? We must remember that the donors in our system are not isolated. Also, the area probed by the measurement is set by the tip-donor layer spacing, which is about 60 nm. Therefore, we are probing a circle of roughly 120 nm diameter. The fact that the average spacing between the dopant in our sample is about 9 nm implies that we simultaneously are probing many dozens of the donor atoms. More importantly, the average spacing is approximately equal to the Bohr radius. Therefore, we cannot evaluate the energies or quantum states of the single dopant atom; our model must include interactions among the dopants. The interactions should be

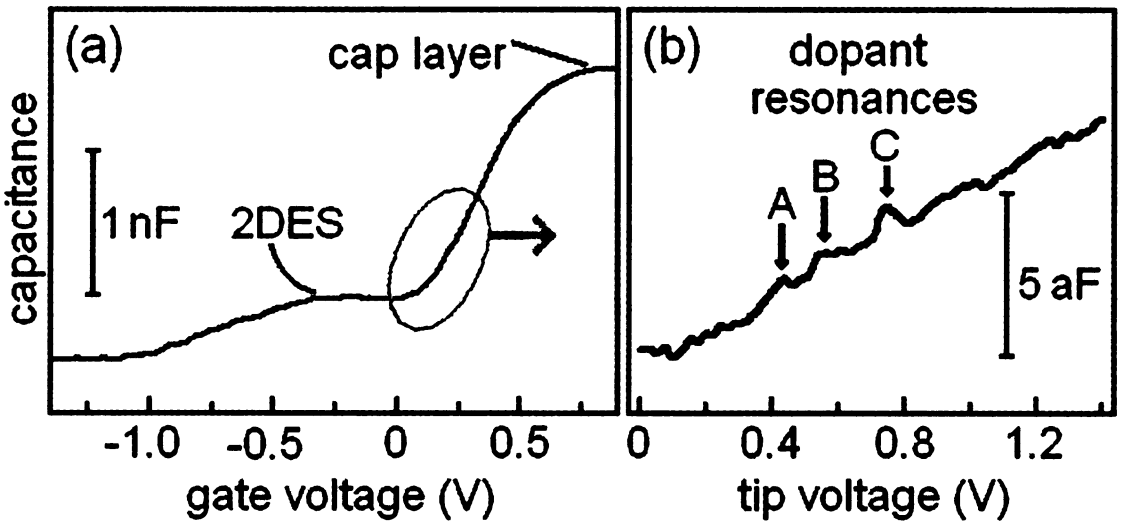

Figure 30. (a) Gated capacitance measurement. The three plateaus that correspond to charge entering different layers in the sample. The area of the gate was 5.7×10^{-7} m^2 (b) Representative capacitance spectroscopy measurement showing the charging spectrum of a system of the dopant atoms below the tip. The black arrows in the plot show the capacitance peaks. The applied excitation voltage was 16 mV and the temperature was 280 mK for both measurements. Due to different α-factors of the two measurements (see text), plot (b) corresponds to probing the voltage range marked by the oval in part (a). The voltages are measured with respect to the nulling voltage, where the gate or tip effectively applies no electric field. Since the energy levels of individuals electrons are too close to be resolved in these voltage ranges, we do not see individual single-electron peaks in these plots.

more important than in the experiments by Geim and coworkers as the density is more than two orders of magnitude higher. To describe our data, we will use both a statistical approach and a simple donor molecule model, for which calculations are within reach.

Figure 31 shows remarkable single-electron tunneling events covering the voltage range of the first electrons to enter the system to peak A. To observe the single electrons, it was necessary to increase the voltage resolution of the measurement, compared to Figure 30(b). This was accomplished by employing smaller voltage increments and a smaller excitation voltage of 3.6 mV rms. The width of the single-electron peaks is set by the AC excitation, if the rms value of the excitation is greater than kT; otherwise the temperature T sets the width. For the low-temperature of 280 mK employed here, we are in the regime where AC amplitude sets the scale.

The expected shape of the peaks is a semi-ellipse [Ashoori]. The inset of Figure 31 compares the measured peak shape directly with the elliptical peak expected for a 3.6 mV rms excitation. The model peak also includes the additional broadening caused by the output filter of the lock-in amplifier. This causes the slight asymmetry in the theoretical peak. Indeed, the measured peaks are very close to the expected shape, consistent with the interpretation that we are probing individual electrons entering the donor layer below the apex of the tip. Based on the magnitude of the individual electron peaks, we can estimate the number of electrons that comprise resonance A, for which individual electrons are not well resolved. This is accomplished by comparing the area of a single-electron peak with the area between peak A and a background line, as shown in Fig. 31. This estimate yields a value of approximately 10. In other words, peak A consists of 10 electrons which tunnel at nearly the same voltage.

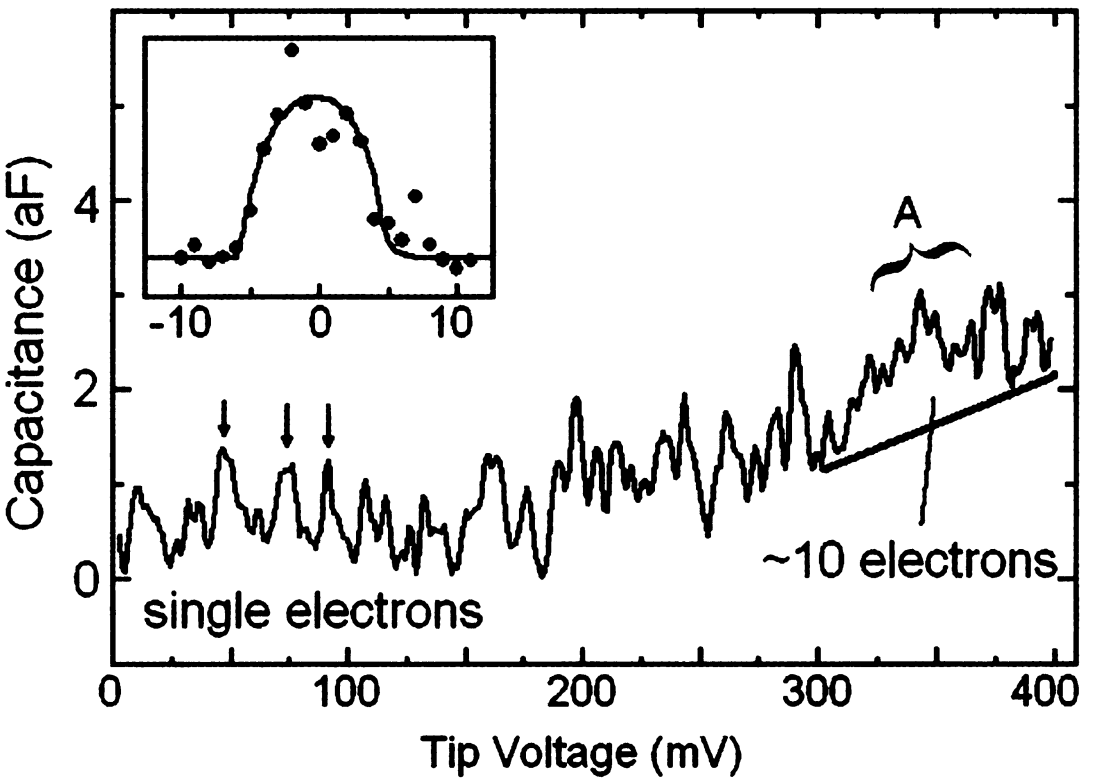

Figure 31. Capacitance versus tip voltage. Three single tunneling events are marked on the curve. The inset shows the comparison of the curve representative of the average of these three peaks (filled dots) with the expected semi-elliptical function (solid curve), as described in the text. Peak A is estimated to be due 10 unresolved electrons, as indicated.

To analyze our data quantitatively, we use a very simple model: we assume that for each dopant atom the energy levels are shifted due to the interaction with its nearest neighbor. Essentially this approach considers the system to be made up of many two-atom "molecules". Clearly, this is a drastic simplification. It ignores larger groupings of atoms and the presence of impurities. Nevertheless, it is a useful approach as a first model. Prof. James F. Harrison at the Michigan State Department of Chemistry applied this model using hydrogenic dopants; the energy levels for different numbers of electrons bound by the two-atom pair were calculated as a function of separation using the configuration interaction method [Sabin&Brandas] to solve Shrödinger's equation. The results are shown in Figure 32; all energies are plotted with respect to the free electron energy. The inset of Figure 32 show a statistical calculation we performed to find the average distance between nearest neighbor dopants. The calculation considered 200 random two-dimensional arrays of dopants, each with the same area as the area probed by our technique and the same density as our actual sample. We see that the average nearest-neighbor separation is 4.65 nm=$0.465a_0$.

To understand how to relate the calculated energy levels to our CAI capacitance measurements, let's consider the tip situated above a single pair of dopant atoms with a separation of $0.465a_0$ (the average nearest-neighbor separation). If the tip voltage is effectively zero, we expect no electrons to tunnel onto the pair. As the tip voltage is made more positive, eventually an electron will tunnel and we will see a peak in the capacitance. This occurs when the electron in the 2DES at the Fermi energy μ has the same energy of the ground state of the molecule. Reading the data off of the "first electron" curve in Fig. 32, we see the predicted energy is E(1)=-3.5 R. A second electron

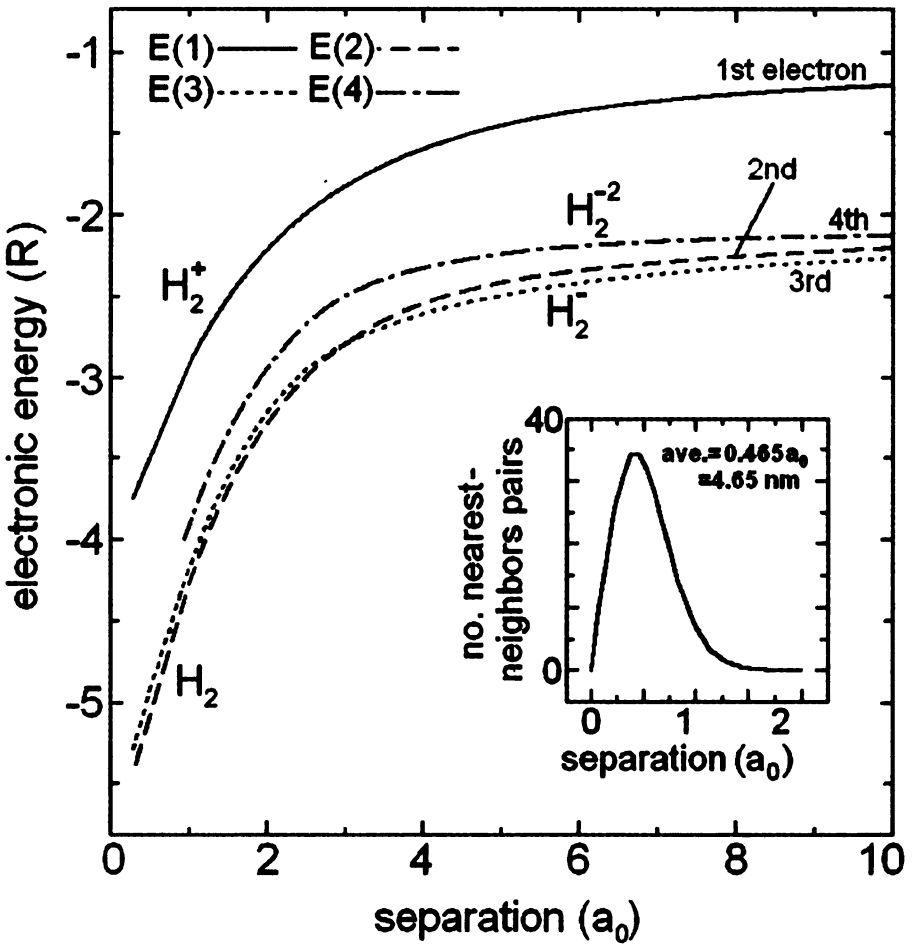

Figure 32. Theoretical ground state electronic energy versus separation for various numbers of electrons on a two-atom potential. These curves were calculated by Prof. J.F. Harrison. Inset: statistical histogram of the nearest neighbor separations. This was calculated using 200 random two-dimensional arrays of dopants, each with the same area as the area probed by our technique and the same density as our actual sample. To make the comparison to the electronic energy calculation more transparent, the results are given in terms of a_0 = 10 nm.

will be trapped by the potential when $\mu+E(1)=E(2)$; i.e. for $\mu=E(2)-E(1)$, where E(2) is the ground state for two electrons in the molecule. Here the calculations predict that the second electron enters at an energy of 5.1 R-3.5 R = -1.6 R. Likewise, the third electron enters when $\mu=E(3)-E(2)$. In this case the theory predicts that the second and third electrons have nearly the same energy. In other words the third electron should be barely bound. Hence, for our measurement it will enter near the free electron energy. Using this same reasoning, the fourth electron is not bound. Therefore, we should observe three peaks as electrons enter the dopant layer. This indeed matches our observation.

If we assume that this model applies, then the voltage corresponding to the free electron energy is given by the voltage of the third peak (peak C), which is 0.75 V on Fig. 30. Next, to compare the predicted peak spacing directly to the observations, we must remember that R = 5 meV and that there is a lever-arm factor that scales the tip voltage by approximately 1/15. Therefore, we expect the first peak at -3.5 R x 5 mV/R x 15 = -0.26 V, relative to the free electron voltage. Likewise, we expect the second peak at -0.12 V, relative to the free electron voltage. In comparison, we observe peak A (the first peak) on Fig. 30(b) at 0.43 V, which is -0.32 V relative to peak C. Peak B (the second peak) occurs at 0.57 V, which is -0.18 V relative to peak C. Hence, peak A occurs at a voltage 60 mV lower than predicted and peak B occurs 60 mV lower than predicted. Scaling these differences back to Rydbergs gives -0.80 R for peak A and 0.80 R for peak B. This agreement is surprisingly good considering the highly simplified nature of the model. Figure 33(a) compares the width of peak A with theory. To generate the theory curve, we used the histogram of nearest-neighbor distances shown in Fig. 32 and scaled

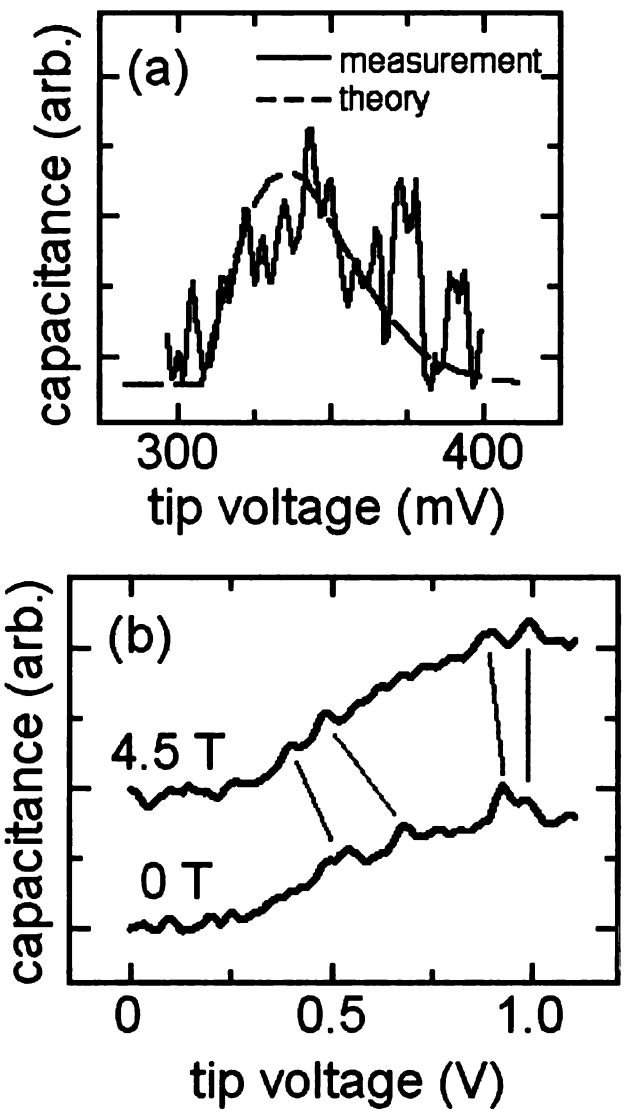

Figure 33. (a) A comparison of measured data (peak A from Fig.31) and the theoretical calculation generated from model shown on Fig. 32 is shown. The widths at half max (FWHM) of these curves agree reasonably well with each other. (b) Capacitance addition spectra at 0 T and at 4.5 T are shown. The shifts that occur at the places of the resonances imply an intriguing behavior of the system.

the horizontal axis using the slope of the E(1) curve at 0.465 a_0. The measured curve is peak A from our high precision data shown in Fig. 31, where we have subtracted the background line, as described above. We see that the width of the two peaks agree reasonably well. Figure 33(b) shows how the peaks shift with magnetic field. Although a theory for this measurement has not yet been developed, it is very interesting to see the behavior of the third peak. It effectively splits into two peaks! In the context of our nearest-neighbor model, this implies that we actually have four electrons that can enter the molecule.

Although our proposed model works surprisingly well, the amplitude of peak A does not agree with simple expectations. In the area probed by the tip, we expect about 140 dopant atoms, or 70 nearest-neighbor pairs. If each pair contributes to the observed peaks, then the peak area should be consistent with 70 electrons. However, as shown in Figure 31, only 10 electrons comprise the peak. This implies that only 10 nearest-neighbor pairs contribute in a way consistent with our model. We speculate that the majority of dopants have significant shifts in their energies due to the close proximity of more than one neighbor. Impurity atoms may also play a role. Another possibility is the presence of deeply bound electronic states known as D_x centers. Dopants in this configuration will not contribute to our measurement as they are effectively permanently occupied by an electron.

In conclusion, we have shown that our scanning probe technique can be a powerful and sensitive method to study a local capacitance of dopants in semiconductors. Our result compare favorably with many of the predictions of a simple model. Clearly more work to be done both experimentally and analytically. For example, to further

investigate the effect of magnetic field on individual resonance peaks magnetic field B could be incremented with small ranges. This is the first probe study of the donor system in semiconductor in tunneling regime with very encouraging and intriguing results.

Chapter 7

Summary and future objectives

7.1 Summary of the investigations

In summary, I would like to point out several important goals have been achieved as a result of this research. First experiments on AlGaAs/GaAs 2D system described in this thesis were building upon the previous work done in our lab [Maasilta, 2003]. It was important for the further understanding of the electronic behavior of the 2D system to study it in a specific regime, searching for the ordered CDW structure and further investigating the effects seen in previous work. The work by Maasilta and coworkers first reported the direct imaging of interior of 2DES the GaAs/AlGaAs with the CAI technique in the tunneling geometry; this effort proved the technique to be a powerful new extension of the original CAI technique that utilize direct ohmic contact to the 2DES [Tessmer 1998, Finkelstein]. This is extremely important since this new technique allows us to resolve 2DES structure near integer filling. The tunneling geometry also provides us with information about the tunneling density of states of the 2DES and is sensitive to the pseudogap physics [Eisenstein, Deviatov, Dolgopolov]. The main focus of the first experiment presented in this thesis was to investigate the density modulation of the 2DES in presence of moderate magnetic fields. In the tunneling geometry, we have observed a characteristic charging behavior of the system near integer fillings. The in-phase component of the capacitance signal showed a diminished signal at integer fillings with the 1/B periodicity which is the quantum mechanical signature of a low-disorder 2DES with a fixed density. The out-of-phase peaks observed at the integer fillings are typically

much smaller features. They do confirm however the variations in tunneling density of states of the 2DES. We believe they arise from correlation effects that modulate the tunneling density of states, which then result in variations in the tunneling resistance at integer fillings.

We have also imaged the density modulations of the 2DES in the tunneling geometry. In this measurement we have concentrated on imaging of ~ 150 nm scale CDW structure that was theoretically predicted to be spontaneously arising near integers and half-integer fillings [Fogler, Koulakov, Shklovskii, Moessner]. To image the bubble and the stripe phases was the primarily goal for us in this experiment. We have observed the evidence of stripe-like structure in 2DES for the magnetic field corresponding to ν=6.5. The length scale of this structure is about 200 nm that is in good agreement with the calculated length scale for this sample. However, we did not observe similar structure for magnetic field corresponding to ν = 4.5 as it was also predicted. The orientation of observed structure at ν=6.5 was approximately 35 degree to the [110] crystalline direction of the host sample. This direction does not support widely accepted concept based on transport measurements, which implies that CDWs tend to orient themselves in the "easy" direction. This direction is a perpendicular to [110] crystalline direction [Lilly, Cooper]. Nevertheless, we find our observation to be a very interesting result that raises several points. For example, an open question is whether the CDW orientation persists to the temperatures at which we performed our measurements, or only fragments of the CDW structure survive. Such fragments do not necessarily exhibit a strong anisotropy but become more isotropic with the increasing temperatures. This idea was also suggested by a transport experiment [Cooper, 2000]. It is still a debated subject and more experimental

and theoretical work could allow for better understanding of the origin of these density modulations.

The topic of our next experimental investigation was to study the charging processes in the delta-donor layer in the same AlGaAs/GaAs heterostructure sample with scanned probe technique. With the first success of this experiment, we have demonstrated an extremely sensitive new way of studying the quantum states of the system. More specifically, we have studied the quantum behavior of the Si^{+}dopant atoms randomly distributed in the δ-doped monolayer. The local capacitance signal from the area below the tip was monitored and the energy levels were evaluated from the capacitance tunneling resonances. This resonances show up as peaks in the capacitance signal. We also resolved remarkably well series of single electron tunneling events at low biases. We attribute the resonances to tunneling through states similar to the D^0 and D^- states of the isolated hydrogen atom model. Our measurements repeatedly show a relatively tall resonance peak and two shorter peaks that occur at lower voltages. Our interpretation of this data is based on the picture of two-atom donor molecules. This is an extreme simplification. For example, clusters of three or more atoms would give rise to deeper states.

Tunneling resonant experiments done by other groups studied the single isolated dopant atom states with resonance tunneling measurements on AlGaAs/GaAs samples have also reported additional features below the threshold of zero bias [Lock, Geim]. However, in most of those experiments the authors were studying an isolated donor atom systems with the donor densities more then two orders of magnitude lower. The features that we observed in our measurements at lower voltages indicate the existence of deeply

bound states that could originate from the presence of impurities in the system or maybe other electronic effects also contribute. Values for the electron binding energies and the width of our capacitance features (peaks) are in a surprisingly good agreement considering the highly simplified nature of our model.

We have also observed the evidence of the magnetic field dependence of our capacitance peaks. It has not been studied fully at present time, but it raises an interesting point: for example, what is the total number of electrons that could be bound in our system, what are their quantum states and how they evolve with applied magnetic field? To continue this discussion more measurements and additional theoretical work is required.

7.2 Future directions

In this work, we have demonstrated that our CAI technique is a powerful method for studying the 2DES and other nanoscale structures. The future directions in this research can be categorized into two main themes. First would be to further continue the study of the 2DES in a quantum Hall regime and explore more about the bubble phase structure, which was not observed in our measurement near integer fillings. Most recent reports indicate a strong resonances in diagonal conductivity σ_{xx} in the microwave regime [Lewis, Chan] near ν=4 1/4 and ν=4 3/4. The authors interpret the resonance as due to a pinning mode of the bubble phase. There is one more very interesting phenomenon that could be studied by imaging the 2DES at high magnetic field on high mobility samples: the "spin bottleneck" phenomenon. Several 3D-to-2D tunneling measurements at magnetic fields near ν = 1 have shown that there are two different tunneling rates for

charge entering the 2DES [Chan, Deviatov, Dolgopolov]. The fast rate is the usual RC charging time. The slower rate is believed to be the spin bottleneck effect, which is a many body phenomenon arising from skyrmion formation in the system [MacDonald]. It reflects a relatively slow electron relaxation time of approximately 1ms. By imaging the 2DES at two different excitation frequencies – one close to the characteristic RC charging time (~ 100kHz) and the other at a much lower characteristic spin bottleneck frequency (~1kHz) – the spin bottleneck effect and the effect on it due to disorder can be studied [Murthy, Brey, Green, Nazarov]. This effect can be resolved in principle with the 3D-2D tunneling CAI technique

There are also new directions building upon the success of our capacitance spectroscopy measurements of donor atoms in the AlGaAs/GaAs samples. The obvious first goal would be to investigate further the magnetic filed dependence of the resonances in the capacitance addition spectra, and develop a complete theory of the effect. There is plenty of motivation to characterize dopant atoms locally. In the context of developing a solid sate quantum computer based on Si atoms, the single dopant atom embedded in a semiconductor crystal represents the smallest possible semiconductor electronic device. At low temperature, the electron or hole can be localized at the parent atom and the quantum state of this charge could play a role of the building bock in the quantum machine – the qubit. For charge based qubits, the qubit-qubit coupling is set by Coulomb interaction, and thus allows for separation of ~100 nm; whereas spin-based qubits have only 10-20 nm coherence length dictated by rapid exponential fall of the exchange interaction [Golding , Kane]. Therefore, the next immediate goal would be to apply the

same scanned probe approach for studying single, isolated atoms in both Si and GaAs based systems. In fact, such project has already been planned in our lab.

REFERENCES

Abraham, D. W., Williams, C., Slinkman, J., Wickramashinghe, H. K., Lateral dopant profiling in semiconductors by force microscopy using capacitive detection., J.Vac. Sci. Technol. B9, 703 (1991).

Ashcroft, N. W., and Mermin, N. D., The Drude theory of metals (Chapter 1), in Solid state physics, 1976, Saunders College, Philadelphia.

Ashoori, R. C., Lebens, J. A., Bigelow, N. P., and Silsbee, R. H., Equilibrium Tunneling from the Two-Dimensional Electron Gas in GaAs: Evidence for a Magnetic-Field Induced Energy Gap, Phys. Rev. Lett. 64, 681 (1990).

Ashoori, R. C., Stormer, H. L., Weiner, J. S., Pfeiffer, L. N., Pearton, S. J., Baldwin, K. W., and West, K. W., Single-Electron Capacitance Spectroscopy of Discrete Quantum Levels, Phys. Rev. Lett. 68, 3088 (1992).

Ashoori, R. C., Electrons in Artificial Atoms, Nature, 379, 413 (1996).

Ballestad, A., Ruck, B. J., Adamcyk, M., Pinnington, T., and Tiedje, T., Evidence from the Surface Morphology for Nonlinear Growth of Epitaxial GaAs Films, Phys Rev. Lett. 86, 2377 (2001)

Becker, A. A., The Boundary Element Method in Engineering, 1992, McGraw-Hill, New York.

Belaidi, S., Gigard, P., Leveque, G. J., Electrostatic forces acting on the tip in atomic force microscopy: Modelization and comparison with analytic expressions, Appl. Phys. 81 (3), 1023 (1997).

Bennett, C. H., DiVincenzo, D. P., Nature 404, 247, (2000)

Besocke, K., An easily operable Scanning Tunneling Microscope, Surf. Sci. 181, 145 (1987).

Binnig, G., Rohrer, H., Gerber, Ch., and Weibel, E., Tunneling through a controllable vacuum gap, Appl. Phys. Lett. 40, 178 (1982).

Binnig, G., In touch with atoms, Rev. Mod. Phys. 71, S234 (1999).

Brey L, Fertig, H. A., Cote, R., MacDonald, A. H., Skyrme crystal in a 2-dimensional electron gas, Phys. Rev. Lett. 75, 2562 (1995).

Caro J, Vink I. D., Smit G., Rogge, S., Direct observation by resonant tunneling of the B+ level in a doped silicon barrier., Phys. Rev. B. 69, 125324 (2004).

Chan, H. B., Ashoori, R. C., Pfeiffer, L. N., West, K. W., Tunneling into ferromagnetic quantum Hall states: observation of a spin bottleneck, Phys. Rev. Lett. 83, 3258 (1999).

Cooper, K. B., Lilly, M. P., Eisenstein, J.P., Jungwirth, T., Pfeiffer, LN, West, K.W., An investigation of orientational symmetry-breaking mechanisms in high Landau levels. Solid State Comm., 119, 89-94 (2001).

Cooper, K. B., Lilly, M. P., Eisenstein, J. P., Pfeiffer, LN, West, K.W., Onset of anisotropic transport of two-dimensional electrons in high Landau levels: Possible isotropic-to-nematic liquid-crystal phase transition, Phys. Rev. B 65, 241313, (2002).

Crook, R., Graham, A.C., Smith, C. G., Farrer, I., Beere, H. E., D. A. Ritchie, D. A. Nature 424, 751 (2003).

Darwin, C. G., The Diamagnetism of the Free Electron, Proc. Cambridge Philos. 27, 86 (1931).

Das Sarma, S., Localization, Metal-Insulator Transitions, and Quantum Hall Effect, in perspectives in Quantum Hall Effects, Edited by S. Das Sarma and A. Pinczuk, John wiley & Sons, New York, 1997.

Davies, J. H., The physics of low dimensional semiconductor, 1998, Cambridge University Press, Cambridge (UK).

Deviatov, E. V., Shashkin, A. A., Dolgopolov, V. T., Hansen, W., Holland, M., Tunneling measurements of the Coulomb pseudogap in a two-dimensional electron system in a quantizing magnetic field, Phys. Rev. B 61, 2939 (2000).

Dolgopolov, V. T., Drexler, H., Hansen, W., Kotthaus, I. P., Holland, M., Electron correlations and coulomb gap in a 2-dimensional electron-gas in high magnetic-fields, Phys. Rev. Lett. 51, 7958 (1995).

Efros, A. L., Density of states of 2D electron gas and width of the plateau of IQHE, Solid State Commun. 65, 1281 (1988).

Efros, A. L., Electrostatics of an inhomogeneous quantum Hall liquid Phys. Rev. B 60

(19), 13343 (1999).

Eisenstein, J. P., Pfeiffer, L. N., and West, K. W., Coulomb Barrier to Tunneling between Parallel Two-Dimensional Electron Systems, Phys. Rev. Lett. 69, 3804 (1992).

Erikkson, M. A., Beck, R.G., Topinka, M., Westervelt, R. M., Campman, K.L., Gossard, A.C., Appl. Phys. Lett . 69, 671 (1996).

Finkelstein G, Glicofridis PI, Ashoori RC, Shayegan M, Topographic mapping of the quantum hall liquid using a few-electron bubble, Science 289 (5476),90 (2000).

Fock, V., Bemerkung zur Quantelung des Harmonischen Oszillator im Magnetfeld, Z. Phys. 47, 446 (1928).

Fogler, M. M. and Koulakov, A. A., Laughlin Liquid to Charge-Density-Wave Transition at High Landau Levels, Phys. Rev. B 55, 9326 (1997).

Fogler, M. M., Koulakov, A. A., Shklovskii, B. I., Ground state of a two-dimensional electron liquid in aweak magnetic field, Phys. Rev. B 54, 1853 (1996).

Geim, A.K., Foster, T.J., Nogaret, A., Mori, N., McDonnell, P.J., LaScala, N., Main P.C., Eaves, L., Resonant tunneling through donor molecules, Phys. Rev. B, (RC), 50 (1994).

Golding, B., Dykman, M. I., Acceptor-based silicon quantum computing, cond-mat/ 0309147.

Gueret, P., Blanc, N., Germann, R., and Rothuizen, H., Confinement and Single-Electron Tunneling in Schottky-Gated, Laterally Squeezed Double-Barrier Quantum- Well Heterostructures, Phys. Rev. Lett 68, 1896 (1992).

Huang, Y., Williams, C., Slinkman, J., Appl. Phys. Lett. 66, 334 (1995).

Huant, S., Najda, S. P., Etienne, B., Phys. Rev. Lett. 65, 1486 (1990).

Holmes, S., Cheng, J.P., McCombe, B. D., Shaff, W, Phys. Rev.Lett. 69, 2204, (1992).

Jackson, J. D. Classical Electrodynamics, John Willey & Sons, New York., (1975), 147-149.

Kane, B. E., A silicon-based nuclear spin quantum computer, Nature, 393, 133 (1998).

Koulakov, A. A., Fogler, M. M., Shklovskii, B. I., Charge Density Waves in Two - Dimensional Electron Liquid in Weak Magnetic Field, Phys. Rev. Lett. 76, 499 (1996).

Kouwenhoven, L. P., Oosterkamp, T. H., Danoesastro, M. W. S., Eto, M., Austing, D. G., Honda, T., and Tarucha, S., Exitation Spectra of Circular, Few-Electron Quantum Dots, Science 278, 1788 (1997).

Kouwenhoven, L. P., Austing, D. G., and Tarucha, S., Few electron quantum dots, Rep. Prog. Phys. 64, 701 (2001).

Kuljanishvili, I., Chakraborty, S., Maasilta, I., Tessmer, S.H., Melloch, M. R., Modeling Electric-Field-Sensitive scanning probe measurements for tip of arbitrary shape, Ultramicroscopy, 102 , 7-12 (2004).

Laughlin, R. B., Quantized Hall Conductivity in Two Dimensions, Phys. Rev. B 23, 5632 (1981).

Laughlin, R. B., Anomalous Quantum Hall Effect: An Incompressible Quantum Fluid with Fractionally Charged Excitations, Phys. Rev. Lett. 50, 1395 (1983).
Likharev, K. K., Proc. IEEE 87, 606 (1999)

Levi, B. G., Scanning Microscopes Probe Local Details of the Quantum Hall State, Physics Today (Search and Discovery) 51(4), 17 (1998).

Lewis, R. M, Ye, P.D., Engel, L.W., Tsui, D.C., Pfeiffer, L, N., West , K. W., Microwave resonance of the Bubble Phases in ¼ and ¾ filled High Landau Levels, Phys. Rev. Lett. 89, 136804, (2002).

Lilly, M. P., Cooper, K. B., Eisenstein, J. P., Pfeiffer, L. N., and West, K. W., Evidence for an Anisotropic State of Two-Dimensional Electrons in High Landau Levels, Phys. Rev. Lett. 82, 394 (1999).

Lok, JGS., Geim A. K., Maan, J.C., D^- centers probed by resonant tunneling spectroscopy, Phys. Rev. B, 53, 9554 (1996).

Maasilta, I. J., Chakraborty, S, Kuljanishvili, I., Tessmer, S. H., and Melloch, M. R., Tunneling images of a 2D electron system in a quantizing magnetic field, Physica E 18, 167 (2003).

Maasilta, I. J., Chakraborty, S, Kuljanishvili, I., Tessmer, S. H., and Melloch, M. R., Direct Observation of Micron-Scale Ordered Structure in a Two-Dimensional Electron System, Phys. Rev. B. 68 (2003).

Martin, Y., Abraham, D. W., C., Slinkman, J., Wickramashinghe, H. K., High-resolution capacitance measurement and potentiometry by force microscopy, Appl. Phys. Lett. 52, 1103 (1988).

Materials Analytical Services, 616 Hutton Street, Suite 101, Raleigh, NC, 27606

MacDonald, A. H., Spin bottlenecks in the quantum Hall regime, Phys. Rev. Lett. 83, 3262 (1999).

Main, P. C., Beton, P. R., Dellow, M. W., Eaves, L., Foster, T. J., Langerak, C. J. G. M., Renini, M., and Sakai, J. W., Transport in Submicron Resonant-Tunneling Devices, Physica B 189, 125 (1993).

Mimura, T., HEMT and LSI application (Chapter 4), in Semiconductor and semimetals, Vol. 30, Academic Press Inc., 1990.

Moessner, R. and Chalker, J. T., Exact Results for Interacting Electrons in High Landau Levels, Phys. Rev. B 54, 5006 (1996).

Movsovich, R., in Experimental techniques in condensed matter physics at low temperature (Sec: 3.3), edited by R. C. Richardson and E. N. Smith, Addison-Wesley, New York, 1988.

Murthy G., Effects of disorder on the nu = 1 quantum Hall state, Phys. Rev.B. 64, 241309 (2001).

Nazarov, Y. V., and Khaetskii, A. V., Quantum phase transition in the skyrmion lattice, Phys. Rev. Lett. 80, 576 (1998).

Neilsen, M. A., and Chuang, I. L., Quantum Computation and Quantum Information, (Cambridge , 2000).

Prange, R. E., Girvin, S. M., The Quantum Hall Effect (2nd Ed.), Springer-Verlag, New York 1987.

Platzman, P., Dykman M. I., Quantum computing with electrons floating on liquid helium, Science 284, 1967 (1999).

Schmidt, T., Tewordt, M., Blick, R. H., Haug, R. J., Pfannkuche, D., and v. Klitzing, K. Quantum-Dot Ground State in a Magnetic Field Studied by Single-Electron Tunneling Spectroscopy on Double-Barrier Heterostructures, Phys. Rev. B 51, 5570 (1995).

Shi, J. M, Peeters, F. M, Devreese, J.T., Phys. Rev. B 51, 7714 (1995).

Shklovskii, B. I., and Efros, A. I., Electronic Properties of Doped Semiconductors, Springer- Verlag, New York, 1984.

Skinner, A. J., Davenport M. E., Kane, B. E., Hydrogenic Spin Quantum Computing in Silicon: A Digital Approach, Phys. Rev. Lett. 90, 087901 (2003).

Smelyansky, V. N., Petukhov A. G., Osipov, V. V., Quantum computation in long lived donor states of Li in Si, quant-ph/0407220.

Smith, T. P., Goldberg, B. B., Stiles, P. J., and Heiblum, M., Direct Measurement of the Density of States of a Two-Dimensional Electron Gas, Phys. Rev. B 32, 2696 (1985).

Sohn, L.L., Kouwenhoven, L. P., Schön, C., Mesoscopic Electron Transport in Semiconductor Nanostructures, (1997), Kluwer Academic, New York.

Stern, F., unpublished internal IBM technical report (1972).

Tarucha, S., Quantum Dots and Artificial Atoms (Chapter 2, Section 2.4), in Mesoscopic Physics and Electronics, Edited by T. Ando, Y. Arakawa, K. Furuya, S. Komiyama, and H. Nakashima. Springer-Verlag, Berlin Heidelberg, 1998.

Tarucha, S., Austing, D. G., Honda, T., van der Hage, R. J., and Kouwenhoven, L. P., Shell Filling and Spin Effects in a Few Electron Quantum Dot, Phys. Rev. Lett. 77, 3613 (1996).

Tessmer, S. R., Glicofridis, P. I., Ashoori, R. C., Levitov, L. S., and Melloch, M. R., Subsurface Charge Accumulation Imaging of a Quantum Hall Liquid, Nature 392, 51 (1998).

Tessmer, S. R., Finkelstein, G., Glicofridis, P. I., Ashoori, R. C., and Melloch, M. R., Modeling subsurface charge accumulation images of a quantum Hall liquid, Phys. Rev. B 66, 125308 (2002).
Topinka, M. A., LeRoy, B.J., Westervelt, R. M., Shaw, S., Fleishman, R., Heller, E. J., Maranowski, K. D., Gossard, A.C., Nature, 410, 183 (2001).

Tsui, D. C., Stormer, H. L., Gossard, A. C., Two-Dimensional Magnetotransport in the Extreme Quantum Limit, Phys. Rev. Lett. 48, 1559 (1982).

Urazhdin, S., Maasilta, I. J., Chakraborty, S., Moraru, I., Tessmer, S. H., High scan area cryogenic scanning probe microscope, Rev. Sci. Instrum. 71, 4170 (2000).

Urazhdin, S., Tessmer, S. H., Ashoori, R. C., A simple low-dissipation amplifier for cryogenic scanning tunneling microscopy, Rev. Sci. Instrum. 73, 310 (2002).

von Klitzing, K., Dorda, G., and Pepper, M., New Method for High-Accuracy Determination of the Fine-Structure Constant based on Quantized Hall Resistance, Phys. Rev. Lett. 45, 494 (1980).

Wigner, E., On the Interaction of Electrons in Metals, Phys. Rev. 46, 1002 (1934).

Yoo, M. J., Fulton, T. A., Hess, H. F., Willett, R. L., Dunkleberger, L. N., Chichester, R. J., Pfeiffer, L. N., and West, K. W., Scanning Single-Electron Transistor Microscopy: Imaging Individual Charges, Science 276, 579 (1997).

Yacoby, A., Hess, H. F., Fulton, T. A., Pfeiffer, L. N., West , K.W, Solid State Commun. 111, 1 (1999).